THESIS FOR THE DEGREE OF LICENTIATE OF ENGINEERING

Modelling of Electric Arc Welding: arc-electrode coupling

ALIREZA JAVIDI SHIRVAN

Department of Applied Mechanics
Division of Fluid Dynamics
CHALMERS UNIVERSITY OF TECHNOLOGY
Gothenburg, Sweden 2013

Modelling of Electric Arc Welding: arc-electrode coupling

ALIREZA JAVIDI SHIRVAN

Thesis for the degree of Licentiate of Engineering 2013:12
ISSN 1652-8565

Department of Applied Mechanics
Division of Fluid Dynamics
Chalmers University of Technology
SE–412 96 Gothenburg
Sweden
Telephone + 46 (0)31 – 772 1000

Typeset by the author using LaTeX.

Chalmers Reproservice
Gothenburg, Sweden 2013

Modelling of Electric Arc Welding: arc-electrode coupling
Thesis for the degree of Licentiate of Engineering in Thermo and Fluid Dynamics
ALIREZA JAVIDI SHIRVAN
Applied Mechanics
Division of Fluid Dynamics
Chalmers University of Technology

ABSTRACT

Arc welding still requires deeper process understanding and more accurate prediction of the heat transferred to the base metal. This can be provided by CFD modelling.

Most works done to model arc discharge using CFD consider the arc core alone. Arc core simulation requires applying extrapolated experimental data as boundary conditions on the electrodes. This limits the applicability. To become independent of experimental input the electrodes need to be included in the arc model. The most critical part is then the interface layer between the electrodes and the arc core. This interface is complex and non-uniform, with specific physical phenomena.

The present work reviews the concepts of plasma and arc discharges that are useful for this problem. The main sub-regions of the model are described, and their dominant physical roles are discussed.

The coupled arc-electrode model is developed in different steps. First coupling solid and fluid regions for a simpler problem without complex coupling interface. This is applied to a laser welding problem using the CFD software OpenFOAM. The second step is the modelling of the interface layer between cathode and arc, or cathode layer. Different modelling approaches available in the literature are studied to determine their advantages and drawbacks. One of them developed by Cayla is used and further improved so as to satisfy the basic principles of charge and energy conservation in the different regions of the cathode layer. A numerical procedure is presented. The model, implemented in MATLAB, is tested for different arc core and cathode conditions. The main characteristics calculated with the interface layer model are in good agreement with the reference literature. The future step will be the implementation of the interface layer model in OpenFOAM.

Keywords: arc welding simulation, plasma, arc discharge, cathode layer, sheath

Acknowledgments

First I would like to express my sincere thanks to my main supervisor associate professor Isabelle Choquet for her huge support and encouragement. Thank you for believing in me and guiding me with patience to find my way in the research field. It is a privilege being your student and I wish I would keep learning from you.

I would like to thank my co-supervisor associate professor Håkan Nilsson for the support and valuable courses, discussions and feedbacks regarding the project and more specifically the OpenFOAM software.

I do appreciate all comments and discussions by my colleagues in the Welding group of Production Technology West at University West in Trollhättan.

The financial support for this work provided by IV-Mechanical Engineering department at University West is acknowledged.

I finally give thanks to my loving wife Salma for her endless kindness and great support and love.

ALIREZA JAVIDI SHIRVAN
Gothenburg, May 2013

Preface

This thesis consists of an extended summary and the following paper:

Paper A

Alireza Javidi Shirvan, Isabelle Choquet, and Håkan Nilsson. Numerical modelling of shielding gas flow and heat transfer in laser welding process. In *Proceedings of The 5th International Swedish Production Symposium, Linköping, Sweden*, pages 269–276, 2012.

Other publications related to the thesis by the author

Publication I (attached in Appendix A)

Isabelle Choquet, Alireza Javidi Shirvan, and Håkan Nilsson. Electric welding arc modeling with the solver OpenFOAM - a comparison of different electromagnetic models. In *International Institute of Welding Document No 212-1189-11,* 2011.

Publication II

Isabelle Choquet, Alireza Javidi Shirvan, and Håkan Nilsson. On the choice of electromagnetic model for short high-intensity arcs, applied to welding. *Journal of Physics D: Applied Physics*, 45(20):205203, 2012.

Contents

Nomenclature

A_{cath}	cross-sectional area of the cathode [m^2]
A_R	Richardson constant (1.2×10^6) [$A \cdot m^{-2} \cdot K^{-2}$]
Ar^j	argon atom (j=0) or ion (j>0) of charge number j [-]
C_p	specific heat at constant pressure [$J \cdot kg^{-1} \cdot K^{-1}$]
e	electron charge (1.602×10^{-19})[C]
E_{Ar^j}	ionization energy of Ar^j [eV]
E_c	surface electric field [$V \cdot m^{-1}$]
E_{ion}	ionization energy [eV]
h	enthalpy [J]
h_p	Planck constant (6.626×10^{-34})[$J \cdot s$]
I	electric current [A]
J	Jacobian matrix
J_{bd}	back diffusion electron current density [$A \cdot m^{-2}$]
J_{cath}	cathode current density [$A \cdot m^{-2}$]
J_{em}	electron emission current density [$A \cdot m^{-2}$]
J_i	ion current density [$A \cdot m^{-2}$]
J_{sem}	secondary electron emission current density [$A \cdot m^{-2}$]
J_{tot}	total current density [$A \cdot m^{-2}$]
k	Boltzman constant (1.380×10^{-23}) [$J \cdot K^{-1}$]

m_e electron mass (9.109×10^{-31})[kg]

n_{Ar^j} number density of Ar^j [m^{-3}]

N_A Avogadro Number (6.022×10^{23}) [mol^{-1}]

n_a atom number density [m^{-3}]

n_e electron number density [m^{-3}]

n_{e-saha} electron density according to Saha law [m^{-3}]

$n_{e\infty}$ electron number density at plasma core [m^{-3}]

n_{es} electron number density at the sheath/pre-sheath interface [m^{-3}]

n_i ion number density [m^{-3}]

P pressure [Pa]

P_{Ar^j} number of energy levels of Ar^j [-]

Q_{Ar^j} partition function of Ar^j [-]

T_c cathode surface temperature [K]

T_e electron temperature [K]

T_h heavy particle temperature [K]

T_i ion temperature [K]

u_e thermal velocity of electrons [$m \cdot s^{-1}$]

U_i voltage drop at pre-sheath layer [V]

u_i thermal velocity of ions [$m \cdot s^{-1}$]

U_s voltage drop at sheath layer [V]

$v_\pm$ max/min ion velocity at the cathode surface [$m \cdot s^{-1}$]

v_s Bohm velocity [$m \cdot s^{-1}$]

Z average ion charge number [-]

α degree of ionization [-]

ΔE_{Ar^j} lowering of ionization energy of Ar^j $[eV]$

ϵ surface emissivity [-]

ϵ_0 electric permittivity in vacuum (8.854×10^{-12}) $[A \cdot s \cdot V^{-1} \cdot m^{-1}]$

γ coefficient of secondary electron current density [-]

κ thermal conductivity $[W \cdot m^{-1} \cdot K^{-1}]$

λ_D Debye length $[m]$

μ viscosity $[Pa \cdot s]$

ϕ work function $[eV]$

ϕ_{eff} effective work function $[eV]$

ρ plasma density $[kg \cdot m^{-3}]$

σ Stefan-Boltzmann constant $(5.670 \times 10^{-8})[W \cdot m^{-2} \cdot K^{-4}]$

Chapter 1

Introduction

Arc welding was introduced into the industrial world at the end of the 19th century. At that time the large amount of electric current needed to weld with an electric arc could indeed be provided. At the beginning the welding arc was generated using a carbon electrode. The carbon electrode was rapidly replaced by other electrode materials, first steel and later tungsten. Tungsten is a refractory material that allows the arc to maintain without melting the electrode. This made it possible to weld with or without filler material. The process is called Tungsten Inert Gas welding (TIG) [55]. This type of welding thus uses a non-consumable electrode and protects the weld from atmospheric contamination by an inert shielding gas. The TIG welding process is now more commonly called Gas Tungsten Arc Welding (GTAW). Another type of welding is the Gas Metal Arc Welding (GMAW) which employs a consumable wire electrode. It has two subtypes: Metal Inert Gas welding (MIG) and Metal Active Gas (MAG). MIG employs an inert gas as TIG. Argon/helium and argon/nitrogen mixtures are common inert gases. MAG, however, uses reactive gases, e.g. argon/carbon-dioxide or argon/oxygen mixture. Active gas is used for some materials like non-alloyed steel, to improve the stabilization of the electric arc and the weld penetration, as well as to increase the welding speed thanks to the larger amount of energy provided by the active gas. These welding processes are summarized in Table 1.1.

	GTAW (TIG)	GMAW (MIG)	GMAW (MAG)
electrode	non-consumable	consumable	consumable
shielding gas	inert $(Ar + He)$ $(Ar + N)$	inert $(Ar + He)$ $(Ar + N)$	active $(Ar + CO_2)$ $(Ar + O_2)$

Table 1.1: Summary of arc welding processes.

Welding plays a leading role among the joining processes in manufacturing industry. However, as with any other manufacturing process, it has its own defects. Common weld defects are lack of fusion, lack of penetration, excess penetration, porosity, undercuts, solidification cracks and spatters. These defects can cause waste because of rejection of the welded piece (when it is possible to notice that the defects are too severe), or an increased risk of failure due to accelerated ageing of the welded piece. Waste saving is also an important issue for developing sustainable production. Many research studies are focused on the discovery and reduction of such defects. A major part of these investigations are experimental. In addition to experimental studies, numerical modelling and simulation methods are also employed to help investigating the effect of process parameters with the aim of improving quality and productivity.

Modelling and simulation of welding include a variety of activities covering the behaviour of the thermal arc heat source, the behaviour of the weld pool, changes in the materials microstructure and properties during welding, and residual stress and temperature evolution of welds. It started in the 1970s with the simulation of residual stress and temperature evolution of welds. Such investigations require assuming an initial temperature distribution resulting from the heat input into the base metal during the welding process. A particular problem is the accuracy of the input data used in the simulation models, such as the material model and the initial temperature distribution. This field is still under development.

Simulation of changes in material micro-structure and properties during welding began in the 1980s. This type of modelling also requires assuming the heat input into the base metal during the welding process. Simulation of microstructure of the material in the welded joint is important to predict the risk of various types of cracks or deterioration of mechanical properties. This field is still under development to investigate new alloys for instance, and further improve the input data in the models. Changes in the material microstructure and properties during welding depend not only on the material composition but also on the cooling rate. The cooling rates are determined experimentally. Very recent works include the effect of cooling and solidification of weld pools, using flow simulations.

The behaviour of the weld pool was started to be simulated during the same decade. Simulations of the weld pool are based on solving the fluid flow equations in the presence of electromagnetic forces. The flow equations are supplemented with an energy equation including phase change (melting/solidification) for temperatures ranging from room temperature to a few thousand Kelvin. Again, the heat input into the base metal during the welding process is needed as input data. In most cases this heat input is specified by imposing a semi-empirical profile involving parameters that are adjusted to closely reproduce the experimental weld geometries.

A Gaussian distribution is taken into account in many computational models through the application of a boundary condition for the heat flux. For example Zhang et al. [57] developed a Gaussian distribution boundary condition of heat flux according to

$$q = \frac{IV\eta}{2\pi r_b^2} \exp\left(-\frac{r^2}{2\,r_b^2}\right) - h_c(T - T_a) - \sigma\epsilon(T^4 - T_a^4) \tag{1.1}$$

where I is the arc current, r is the radial coordinate and V is the arc voltage. The problem with this approach is that there are four parameters that should be estimated. (1) The arc efficiency, η, (2) the convective heat transfer coefficient, h_c, (3) the arc temperature adjacent to the work-piece, T_a, and (4) the heat distribution parameter, r_b. The arc efficiency has a direct effect on the magnitude of the heat flux. Vast number of welding parameters like arc current, shielding gas composition, arc length, welding speed and electrode tip angle influence the arc efficiency. This makes it difficult to achieve an accurate estimation of the arc efficiency. For example, for the GMAW process an arc efficiency between 0.22 and 0.8 can be found in different reports [51]. The last three parameters also depend on many other parameters which can change for each particular case. An advantage of this model is its simplicity. A drawback is the need of experimental data to set the unknown parameters case by case. An alternative would be to use the heat input data provided by an arc heat source simulation model. The link with research work for modelling the heat source is still in its infancy.

The most recent area is the simulation of the welding arc heat source, i.e. the thermal plasma. This thermal plasma is basically modelled by coupling thermal fluid mechanics (governing mass, momentum and energy or enthalpy) with electromagnetics (governing the electric field, the magnetic field, and the current density) for temperature ranging from room condition to about $30000K$.

The first simulation model coupling thermal fluid mechanics and electromagnetics to simulate the entire plasma core of an axi-symmetric high-intensity electric arc was developed by Hsu et al. in 1983 [30]. The arc investigated in this pioneering study was rather far from the welding arcs used in production. Since the late 1990's many developments have been done to further improve the modelling of the arc heat source in the particular context of welding. A review can be found in the thesis by Sass-Tisovskaya [48]. The arc heat source simulation can improve the understanding of the process in the arc, and thereby increase the opportunities to control the process better. It can also provide the heat input data needed by the other, above-mentioned, welding research domains.

The aim of this work is to take one step further towards the coupling of the plasma arc heat source and the metal (both electrode and base metal, with melting). The step investigated here is the arc-electrode coupling. A few authors have worked on this topic for welding arcs, but none of them are using the same

model. Further investigations are thus needed to clarify this situation. To do so we first recall some general plasma properties useful for specifying the context of this work.

1.1 Plasma

Plasma is a globally electrically neutral gas, in which a certain portion of the particles are ionized. Just as a standard gas, plasma does not have an exact shape except when surrounded by a container. However, plasma may adopt a specific shape under the influence of a magnetic field. A plasma is a distinct phase, separated from the gas phase, mainly due to its collective behaviour. The charged particles are neither bounded nor free. As they do interact via long-range interactions, i.e. Coulomb interaction, they respond strongly to electromagnetic fields. The moving charged particles induce an electric current and a magnetic field, by which they influence each other. This collective behaviour, specific to plasma, can be observed if the distance among the charged particles is short enough so that the particles interact at some distance, rather than just with the closest ones. This criteria, called **plasma approximation**, is valid when the number of charged particles within a sphere of radius equal to the Debye length is larger than unity [18, 29]. In an argon plasma for instance, **the Debye length** (λ_D) is the distance at which the electrons do screen a positively charged argon ions. Assuming that electron and ion temperature can be defined, the Debye length is given by [21]

$$\lambda_D = \sqrt{\frac{\epsilon_0}{e^2(n_e/T_e + n_i/T_i)}}$$

where ϵ_0 is the electric permittivity in vacuum, e is the electron charge and n_e, n_i are the number densities of electrons and ions respectively and T_e and T_i are their temperatures. The number densities n_e and n_i also allow defining the **degree of ionization** of a plasma. It represents the proportion of atoms or neutral particles that have lost (or gained) electrons. The degree of ionization can be described as

$$\alpha = n_i/(n_i + n_a)$$

where n_i is the total number density of ions and n_a number density of neutral atoms. Plasma is usually classified as hot when fully ionized, e.g. a supernova, or as cold when partially ionized (even small fraction. i.e. 1%), e.g. a lightning or an aurora. Most man-made cold plasmas are in the range of 10^6 to $10^8 electron/cm^3$ for the electron density and between 0.1 to $20eV$ for the electron energy. It should be noted that, despite the name, the electron temperature in a cold plasma can reach several thousand degree Kelvin. With regard to

this definition most of the plasma tools in manufacturing technology, including electric arc welding, are cold plasma. Cold plasma is further classified as thermal and non-thermal. Thermal plasma refers to a plasma in which electrons and heavy particles temperature are of the same order. Non-thermal plasma on the other hand have heavy particles at low temperature (almost room temperature) while the electron temperature can be several order higher. A thermal plasma can be formed using a magnetic field, which is called magnetically induced plasma [24]. In welding application it is more common to form thermal plasma heating and ionizing a gas by driving an electric current through it. It then belongs to the family of electric discharges.

1.2 Electric discharges

To form an electric discharge a voltage V can be applied between two separate electrodes.

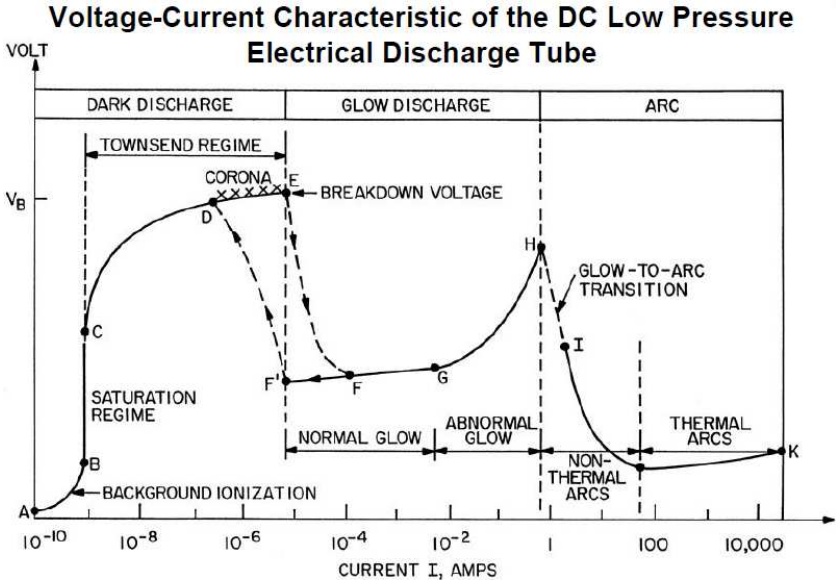

Figure 1.1: Example of characteristic curve of the electric discharge (non specified gas) [47]

Figure 1.1 shows the three types of discharges that can be developed, depending on voltage, V, and current, I, through the plasma. Each type of discharge can be further divided into subtypes, as shown below, where the characteristic data given in brackets corresponds to an argon plasma at atmospheric pressure [10].

1. **Dark discharge**: This type of discharge is invisible to the eye, except for Corona regime.

   (a) Background ionization regime: ($10^{-10} \leqslant I < 10^{-9} A$)

   (b) Saturation regime: ($I = 10^{-9} A$)

   (c) Townsend regime: ($10^{-9} < I < 10^{-5} A$)

   (d) Corona discharge: visible radiation start being emitted.

2. **Glow discharge:** This type of discharge is visible and cold (T is of the order of room temperature).

   (a) Normal glow regime: ($10^{-5} \leqslant I < 10^{-2} A$)

   (b) Abnormal glow regime: ($10^{-2} \leqslant I < 1A$)

3. **Arc discharge:** This type of discharge is visible and can be thermal or non-thermal. In the thermal case, the largest temperature observed was about $50000K$. It was measured in a lightning. In GTAW and GMAW the largest temperature does not use to exceed about $25000K$.

   (a) Non-thermal regime: ($0.1 \leqslant I < 10A$)

   (b) Thermal regime: ($I \geq 10A$)

The arc discharge in the thermal regime is the operating principle of electric switchers. It is also involved in material processing based on energy transfer such as plasma cutting, thermal plasma spray and welding. According to this description, it can be argued that electric arc welding is in the frame of cold plasma and the discharge type is the thermal arc discharge.

1.3 Outline of this work

The present work is a continuation of the work by Sass-Tisovskaya [48], on the modelling, implementation, and simulation of GTAW arc considering only the arc core. The equations solved in the arc core model are mass conservation, momentum conservation accounting for the Lorenz force, enthalpy conservation with a Joule heating source term and Maxwell equations [48]. The model was applied to the simulation of a reference GTAW test case using two different magnetic field models: a three-dimensional model and the two-dimensional axi-symmetric model called "electric potential model" which is commonly used in welding arc simulation. According to the literature [43] these two models should have provided the same simulation results when applied to an axi-symmetric arc. But the comparison done by Sass-Tisovskaya [48] revealed a clear deviation in the results. At that time, the exact nature of this problem was not fully understood.

Going back to the complete system of Maxwell equations, deriving the electromagnetic model in the particular frame of a welding arc, it was observed that the so-called electric potential model is based on an assumption that was "forgotten" by most of the community. The model assumes that the radial component of the current density is negligible. Simulations show that this assumption is not valid within the frame of the arcs used in welding. These results are presented in Publications I [33] and II [11]. Publication I is useful for the motivation of the present study, and is attached in Appendix A.

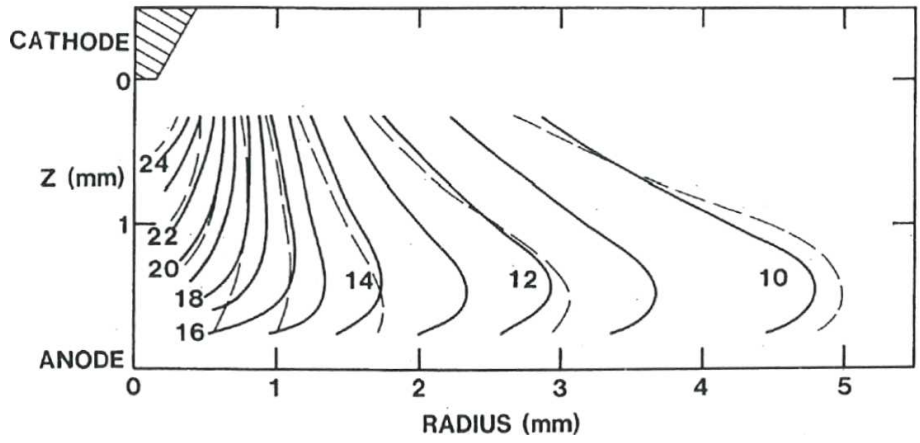

Figure 1.2: Temperature measurements of [26] courtesy of A.J.D. Farmer. Solid lines show results of a GTAW torch burning to a water cooled anode, dashed lines show results of a free-burning arc in an enclosed chamber.

The aim of the present work is to go one step further, including the anode and cathode into the simulation model. The arc models which are just considering the plasma core require some boundary conditions set on the cathode and anode surfaces. These boundary conditions are very difficult to measure experimentally. Only few documented cases are available. An example is shown in Figure 1.2. It was obtained by Haddad and Farmer [26] doing spectroscopic measurements in a steady gas tungsten argon arc on a water cooled copper base metal. The measurements cannot be done in the vicinity of the anode and cathode surfaces since there the control volume available for observation is too small. As a result, the data need to be extrapolated up to the cathode and anode surface to be able to infer the boundary conditions. Such extrapolations are obviously highly inaccurate. The influence of different boundary conditions set in the literature for this test case can be seen in Publication I, Appendix A, (Figures 15-17, cases a and b).

Thus, a comprehensive model including the anode and cathode in the arc model should be established. Comprehensive model refers to a model based on fundamental physics and independent of parameters imported from experiments.

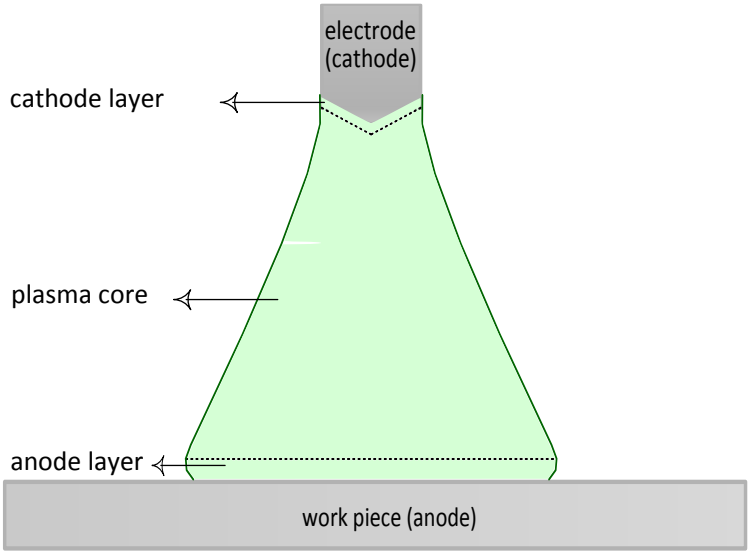

Figure 1.3: Schematic sketch of sub-regions in GTAW

Including the anode and cathode also implies including the anode and cathode layers ensuring the coupling with the plasma core, see Figure 1.3.

The interface layers between the electrode and the thermal plasma core are complex to model. One source of complexity is due to their non-uniformity. For this reason the plasma arc discharge is commonly divided into sub-regions, each sub-region is characterized by specific leading physical phenomena. These sub-regions and some of their properties important for the model are presented in chapter 2.

The development of this comprehensive arc model including the anode and cathode is done in several steps: first a thermal solid-fluid model with a standard coupling is tested. Second the coupling model specific to thermal arc is prepared and tested. For the first step, the OpenFOAM open source solver, chtMultiRegionFoam, is employed to make the thermal coupling between a solid and a flowing fluid. This solver is first applied to a simple application of laser welding, with shielding gas but neglecting metal melting [33]. The main reason for choosing laser welding is that it does not require any advanced model for coupling the shielding gas to the solid, contrary to arc welding. The results are reported in Publication I, Appendix A, and summerized in chapter 3.

The second step concerns the modelling of the interface layer coupling the arc core and the solid acting as electron emitter or collector that is the cathode and anode respectively. This part will focus more specifically on the cathode layer of a refractory cathode, as used in GTAW. It should be noted that plasma core-anode coupling obeys a similar concept as plasma core-cathode coupling [6, 27, 36]. Therefore, the plasma core-anode coupling can be modelled as a

plasma core-cathode with some modifications. The extension of the interface layer (or cathode layer) model to the non-refractory electrodes used in GTAW would imply changing the law defining the current density emitted by the cathode and accounting for melting and vaporization of both anode and cathode. The problem raised by cathode layer modelling and the main existing models are presented in Chapter 4. The model and the numerical method used in this study are presented in Chapter 5. The calculation results obtained based on the cathode layer model are presented in chapter 6. The conclusion are given in chapter 7, together with suggestions on future work.

Chapter 2

Physics of electric arcs applied to welding

Electric arc discharge is complex to model. A source of complexity is due to its non-uniformity. The dominant physical phenomena are not the same throughout the arc. For this reason the plasma arc discharge is commonly divided into subregions characterized by specific leading physical phenomena, as sketched in Figure 1.3. The main subregions are:

- The solid region (that may be partially melted). It includes the work piece and the electrode. In GTAW welding the electrode is usually the cathode and the work piece is the anode. In GMAW it is usually the opposite.
- The plasma core.
- The interface between cathode and plasma which is called cathode layer.
- The interface between anode and plasma or anode layer.

The ionization degree is an important parameter used in kinetic theory [14, 10] to determine the leading order collisional phenomena taking place in the plasma. Figure 2.1 shows the densities of the different species present in an argon plasma in local thermal equilibrium and at atmospheric pressure. Figure 2.2 shows the corresponding ionization degree. The calculation was done assuming that the ionization energy is provided by the free electron alone, using the Saha law proposed by Van de Sanden [54], as further detailed in section 5.2.1. Although a thermal plasma is partially ionized, it may however be locally highly ionized in the hottest regions, as illustrated in Figure 2.2. When increasing the electron temperature from $5000K$ up to $30000K$, the argon atom number density decreases by almost five orders of magnitude down to $10^{19} atoms/m^{-3}$. The ionization degree is then large, but argon atoms are still present. Besides charged and neutral particles, the plasma species can be classified into light species (electrons) and

heavy species (neutral and ionized atoms/molecules). Due to the significant mass difference, electron-heavy particle collisions are less efficient at transferring momentum and energy than electron-electron or heavy-heavy particle collisions. In regions with high degree of ionisation ($\alpha \geq 10^{-1}$ and $T_e \geq 10000K$ in Figure 2.2), the collision frequency between light and heavy species is large enough to balance the poor efficiency of the momentum and energy transfer. Local thermal equilibrium (LTE) between all the species can then be reached. This property is commonly accepted in thermal arc modelling, and it is supported by model derivations done using kinetic theory [13] and by experimental observation [52]. When going to temperatures below $10000K$, and an ionization degree of the order of $10^{-1} - 10^{-3}$, the reduction in the number of electrons present in the plasma leads to a too low collision frequency to maintain local thermal equilibrium between heavy and light particles. When encountered in the colder regions of the plasma core and in the pre-sheath, the frequency of electron-electron and heavy-heavy particle collisions is still large enough to allow the light species reaching a local thermal equilibrium and the heavy species another one. This situation called non-LTE or partial-LTE depending on the authors, results in a two-temperature model, as derived in [13] using the kinetic theory and assuming that the ionisation energy is provided by free electrons. It is however known [22] that the excited electronic states of the ionized particle also contribute to the ionization energy. This contribution is important in the colder regions of the arc with low electron density. However, there is not yet a satisfying generalization of the Saha law accounting for this contribution.

In practice the plasma core of welding arcs is in most cases modelled using a one-temperature model (LTE). This modelling could be questioned in the colder plasma edges, but as above mentioned there is not yet a satisfying generalization of the Saha law for the colder regions. As a result the calculation of the plasma composition, needed for deriving the thermodynamic and transport coefficients of the two-temperature fluid model is still an open problem.

2.1 LTE Plasma core

The plasma core represents the main body of the plasma. In welding applications it is of the order of $10^{-2}m$ [12]. This region is in the present work assumed to be in local thermodynamic equilibrium (LTE). The plasma core model applies to a Newtonian fluid, assuming:

- a one-fluid model,
- in local thermal equilibrium,
- thermally expansible and mechanically incompressible,

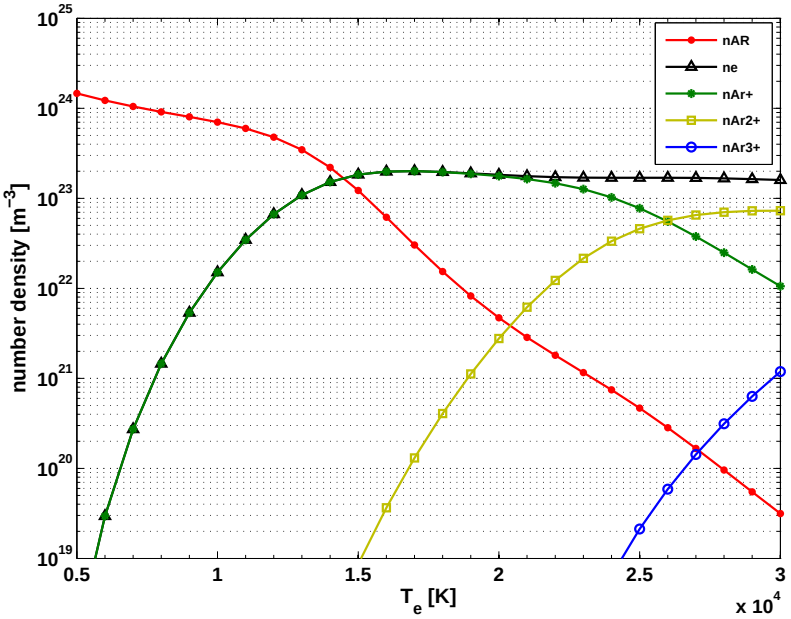

Figure 2.1: Number densities for argon plasma at atmospheric pressure

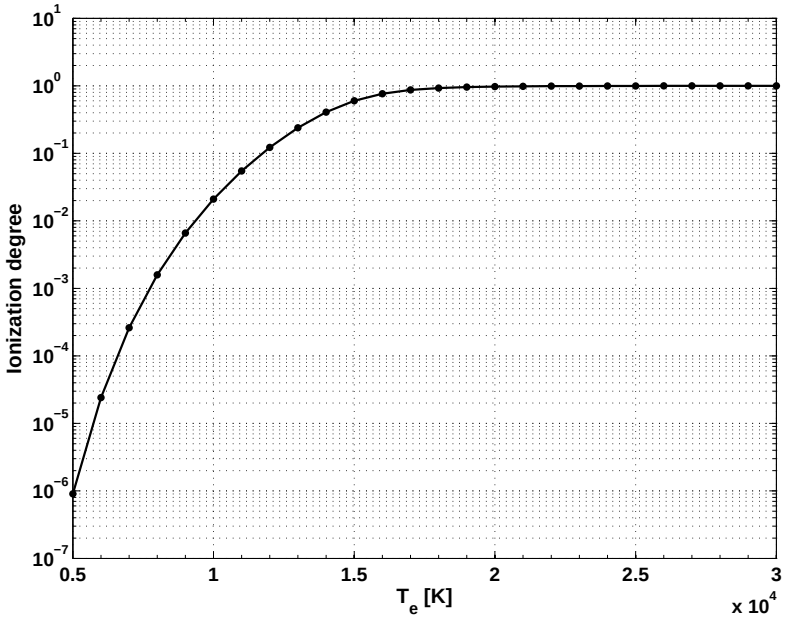

Figure 2.2: Ionization degree for argon plasma at atmospheric pressure

- a laminar flow.

In this framework the continuity equation is written as

$$\frac{\partial \rho}{\partial t} + \nabla \cdot [\rho \, \mathbf{u}] = 0 \, , \tag{2.1}$$

where ρ denotes the fluid density, and $\mathbf{u}$ the fluid velocity. The operator $\nabla\cdot$ denotes the divergence operator. The density $\rho = \rho(T)$ depends on the temperature T, as illustrated for an argon plasma at $1atm$ in Figure 2.3. Pressure dependency can generally be omitted in standard welding applications. However, this simplification is not valid for some other thermal arc applications, such as high power electric arc switchers.

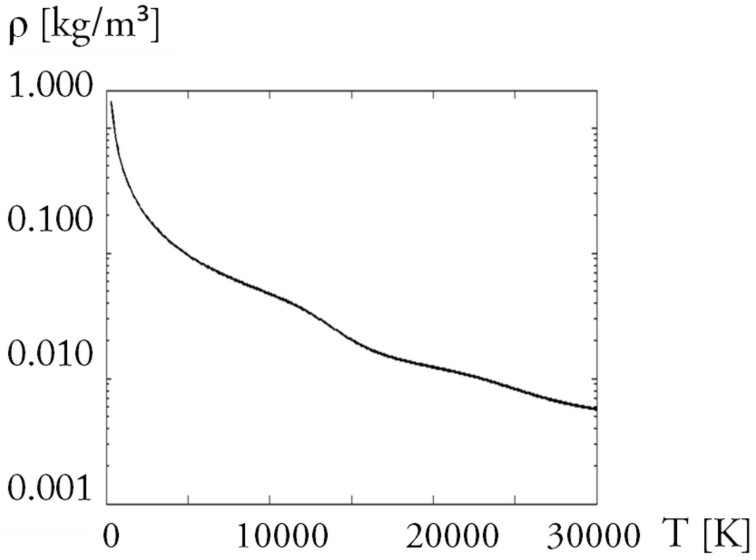

Figure 2.3: Argon plasma density as a function of temperature, plotted based on data derived by Rat et al. [44].

The momentum conservation equation is expressed as

$$\begin{aligned} &\frac{\partial \rho \mathbf{u}}{\partial t} + \nabla \cdot \left[\rho \, \mathbf{u} \otimes \mathbf{u}\right] - \nabla \cdot \left[\mu \left(\nabla \mathbf{u} + (\nabla \mathbf{u})^T\right) - \tfrac{2}{3} \, \mu \, (\nabla \cdot \mathbf{u}) \, I\right] \\ &= -\nabla P + \mathbf{J} \times \mathbf{B} \, , \end{aligned} \tag{2.2}$$

where $\mu = \mu(T)$ is the temperature dependent viscosity, I the identity tensor, P the pressure, $\mathbf{J}$ the current density and $\mathbf{B}$ the magnetic flux density (simply called magnetic field). $\nabla\cdot$ denotes the gradient operator, and $\otimes$ the tensorial product. The last term on the right hand side of (2.2) is the Lorentz force. The enthalpy conservation equation is given by

$$\frac{\partial \rho h}{\partial t} + \nabla \cdot \left[\rho \mathbf{u} \, h\right] - \nabla \cdot \left[\frac{\kappa}{C_p} \, \nabla h\right] = \mathbf{u} \cdot \nabla \cdot P + \mathbf{J} \cdot \mathbf{E} - Q_{rad} + \nabla \cdot \left[\frac{5 \, k_B}{2 \, e \, C_p} \, \mathbf{J} h\right] , \tag{2.3}$$

where h is the specific enthalpy, $\alpha = \alpha(T)$ the temperature dependent thermal diffusivity, $Q_{rad} = Q_{rad}(T)$ the radiation heat loss, k_B the Boltzmann constant, e the elementary charge, $\mathbf{E}$ the electric field and $C_p = C_p(T)$ the temperature dependent specific heat at constant pressure (see Figure 2.4). The third term on the right hand side of equation (2.3) is the Joule heating, and the last term the transport of electron enthalpy. The temperature, T, is derived from the specific enthalpy via the definition of the specific heat,

$$C_p = \left(\frac{dh}{dT}\right)_P . \tag{2.4}$$

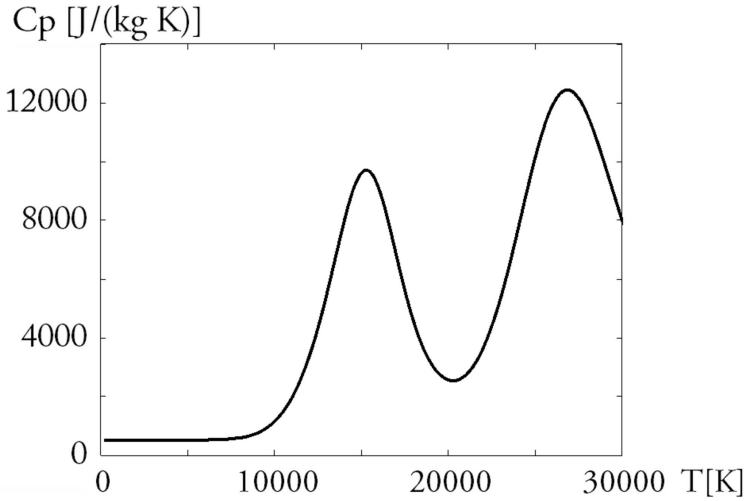

Figure 2.4: Specific heat as a function of temperature for argon plasma, plotted based on data derived by Rat et al. [44].

The electromagnetic model is derived from the set of Maxwell equations, supplemented by the equation governing charge conservation, as further detailed by Sass-Tisovskaya et al. [48]. When considering the core of a thermal arc as used in welding, while ignoring the anode and the cathode sheaths, it can be assumed that

- The Debye length λ_D is much smaller than the characteristic length of the welding arc, so that local electro-neutrality is verified, $q_{tot} = 0$, and the diffusion and thermodiffusion currents due to electrons are small compared to the drift current.
- The characteristic time and length of the welding arc allow neglecting the displacement current $\mu_0 \partial \mathbf{E}/\partial t$ compared to the current density $\mathbf{J}$ in Ampère's law, resulting in quasi-steady electromagnetic phenomena, $\partial \mathbf{E}/\partial t = 0$, and $\partial \mathbf{B}/\partial t = 0$.

- The Larmor frequency is much smaller than the average collision frequency of electrons, implying a negligible Hall current compared to the drift current.
- The magnetic Reynolds number is much smaller than unity, leading to a negligible induction current compared to the drift current.

Based on these assumptions, it is known that there exist a scalar electric potential V and a vector magnetic potential $\mathbf{A}$ defined up to a constant [11]. The electromagnetic system of equations can then be reduced to the Poisson scalar equation governing the electric potential V

$$\nabla\cdot\left[\sigma\,\nabla V\right]=0\,, \tag{2.5}$$

and the vector Poisson equation governing the magnetic potential, $\mathbf{A}$

$$\triangle\mathbf{A}=\mu_o\,\sigma\,\nabla V\,, \tag{2.6}$$

where $\triangle$ denotes the Laplace operator. σ is the electric conductivity and μ_o is the permeability of vacuum. $\mathbf{A}$ is assumed to satisfy Lorentz gauge, $\triangle\mathbf{A}=0$. The current density $\mathbf{J}$, electric field $\mathbf{E}$ and magnetic field $\mathbf{B}$ are then simply derived from the electric and magnetic potential via

$$\mathbf{J}=\sigma\,\mathbf{E}\,. \tag{2.7}$$

$$\mathbf{E}=-\nabla V\,, \tag{2.8}$$

and

$$\mathbf{B}=\nabla\times\mathbf{A}\,. \tag{2.9}$$

where $\nabla\times$ denotes the curl operator. For high-intensity arcs the electric conductivity σ is temperature dependent, as illustrated in Figure 2.5 for an argon plasma using data derived by Rat et al. [44]. The two other extended regions are the anode and the cathode. The cathode layer is further divided into a space charge layer or sheath, and an ionization layer or pre-sheath, as shown in Figure 2.6. The cathode region and its interaction with the plasma core through the cathode layer are now described.

2.2 Cathode

This electron emitter is mostly solid in GTAW, and it is usually partly liquid in GMAW. It should be noted that in this study, the melting of the cathode is not taken into account. In this region the governing equations concern the electric potential, V, the magnetic potential $\mathbf{A}$ and the thermal energy. When phase

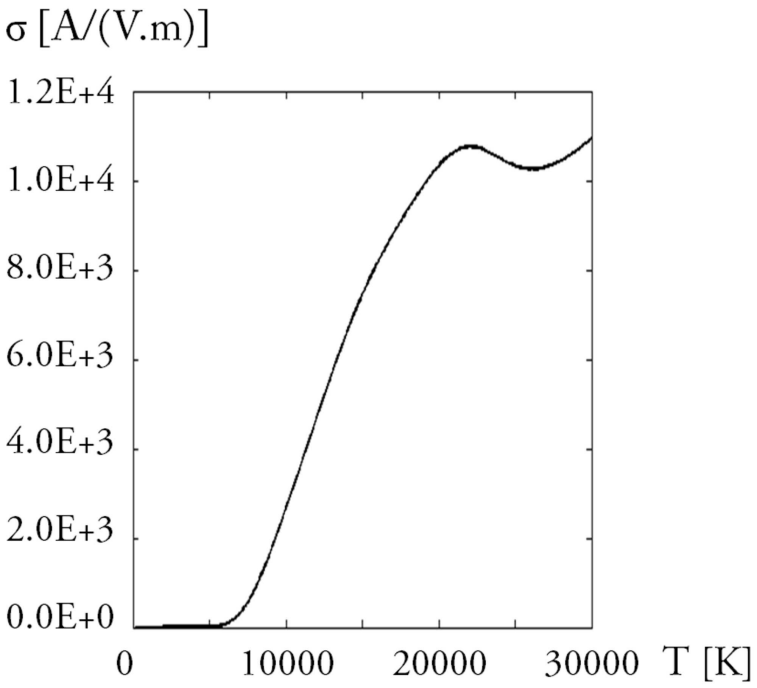

Figure 2.5: Argon plasma electric conductivity as a function of temperature, plotted based on data derived by Rat et al. [44].

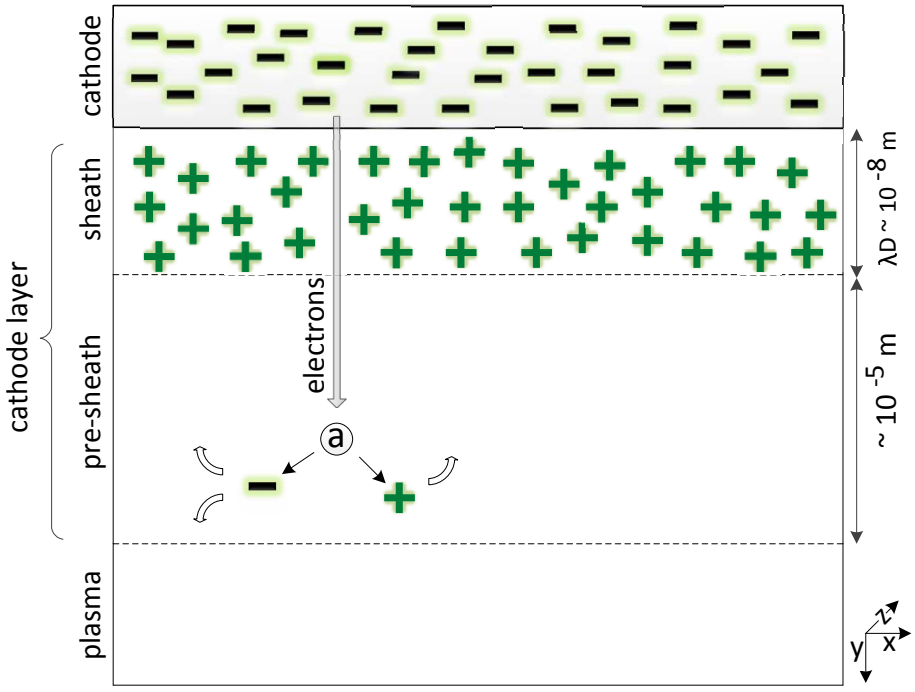

Figure 2.6: Scheme of sub-regions of an arc discharge

change is not included, the thermal energy equation is usually expressed as a temperature equation. When phase change (solidification/melting) is included into the model, an enthalpy formulation is more suited for ensuring energy conservation. The system of equations to be solved in the cathode bulk (assuming no phase change) is thus

$$\nabla \cdot [\sigma_c \, \nabla V] = 0 \, , \tag{2.10}$$

$$\triangle \mathbf{A} = \mu_o \, \sigma_c \, \nabla V \, , \tag{2.11}$$

and also

$$\frac{\partial \rho h}{\partial t} + \nabla \cdot \left[\rho \mathbf{u} \, h\right] = \nabla \cdot \left[\frac{\kappa_c}{C_c} \, \nabla h\right] + \mathbf{J} \cdot \mathbf{E} \tag{2.12}$$

where

$$\mathbf{J} = \sigma_c \, \mathbf{E} \, . \tag{2.13}$$

$$\mathbf{E} = -\nabla V \, , \tag{2.14}$$

$$\mathbf{B} = \nabla \times \mathbf{A} \, . \tag{2.15}$$

The cathode is thus characterized by three main bulk quantities: its thermal conductivity κ_c, its electric conductivity σ_c and its specific heat C_c.

Additional surface material properties are also needed for modelling the cathode ability to emit electrons:

- The work function ϕ.
- The emitted electron current density J_{em}.

The work function of a metal can be defined as the minimum energy that must be given to a valance electron moving freely inside the metal to be liberated from the metal surface. With this minimum energy the electron has no kinetic energy for moving further away from the surface. Also, in this definition of the work function, the valence electron occupies the highest energy level (when the system is in its ground state), which is the Fermi level of energy E_f. An electron escaping with a minimum energy causes a negative charge just outside the metal surface. In return, a positive charge just inside the metal surface is formed. This causes a sheet of dipoles at the metal surface, implying a repulsive force acting upon the electrons as they try to escape from the metal surface. This repulsion force forms a surface potential barrier of energy $E_{vac}(s)$, called the energy vacuum level, close to the surface. The minimum energy for valence electrons to escape the metal and overcome the surface potential barrier is thus

$$\phi = E_{vac}(s) - E_f. \tag{2.16}$$

This energy is called the work function. It is usually expressed in eV and for metal it uses to be between about 1.5 and $6 \; eV$. If a layer of positive ions builds

up outside the metal surface on the top of the dipole layer, as in the sheath or space charge layer of a cathode layer (see section 2.3) it facilitates the electron emission by lowering the surface potential barrier.

Research on electron emission from cathode surfaces started in 1901 with Richardson. It was long believed that all thermal arcs emit electrons by thermoionic emission, i.e. from a large thermal energy input. However, thermoionic emission is not sufficient to explain the large current densities observed experimentally. Other emission processes were then discovered [25]. Among them, two are of importance in arc welding: thermal-field emission, and field emission. The leading emission process type is related to the cathode material properties [53].

The cathodes used in GTAW are made of refractory material. A typical example of refractory cathode is a tungsten cathode; its melting point is $T_m = 3410°\mathrm{C}$, and its boiling point $T_b = 5660°\mathrm{C}$. Refractory materials can sustain high temperature without strong melting or vaporization. Vaporization is thus assumed to be negligible. For refractory material, thermo-field emission is the dominant emission process. Thermo-field emission is thermoionic emission enhanced by the lowering of the surface potential barrier due to the presence of a space charge layer. However, most of the studies ignore the field-enhancement and assume thermoionic emission. The electron emission current density for thermoionic emission is modelled by the Richardson-Dushman equation (5.2). Its field enhancement is accounted for with a correction for the so called Schottky effect, see equation (5.3).

For the non-refractory cathodes, as used in GMAW, a different emission process is dominant: field emission. A typical example of non-refractory cathode is a copper cathode (melting point $T_m = 1083°\mathrm{C}$, boiling point $T_b = 2567°\mathrm{C}$). Non-refractory materials cannot sustain very high temperature. As the cathode surface temperature is lower for non-refractory materials than for refractory, the thermoionic emission is also less efficient. The field emission is then the emission process allowing to maintain a reasonable level of electron emission. In that case the cathode layer (more specifically the space charge layer) is more important. It further lowers the surface potential barrier and also make it thicker, allowing electron tunnelling. Field emission current density is modelled by the Fowler-Nordheim equation [19]. As non-refractory cathodes significantly melt and vaporize, their cooling by vaporization cannot be neglected, while it is usually negligible for refractory cathode.

To calculate the emitted electron current density, we need to know (i) the cathode surface temperature, T_c which requires knowing the net heat flux transferred to the cathode surface, q_{tot} and (ii) the potential drop across the space charge layer, U_s.

2.3 Space charge layer (cathode sheath)

The negative charge forming the surface potential barrier on the cathode surface attracts positive ions, leading to the formation of a positive space charge region shielding the neutral plasma core from the negative cathode wall, see Figure 2.6. This thin region is called space charge layer, or sheath, and its thickness is of the order of the Debye length (almost $10^{-8}m$) [8]. The sheath plays an important role in the cathode layer function [56]:

- It forms a potential barrier that enhances electron emission by lowering the surface potential barrier.
- It accelerates the emitted electrons, pushing them further away from the cathode surface (towards the pre-sheath or ionization layer) and provides them with sufficient kinetic energy to allow promoting impact ionization as they reach the pre-sheath, and thus sustain the discharge.
- It accelerates the ions generated in the ionization layer towards the cathode. These ions heat the cathode up to thermoionic emission temperature by transferring their kinetic energy to the cathode surface during cathode wall collisions. Among these ions, the most highly energetic may also promote secondary emission.
- It forms a potential barrier that reduces the back diffusion of the electrons towards the cathode.

The charge fluxes taking place in the sheath are thus: the flux of electrons emitted from the cathode surface by thermal-field emission and by secondary emission, and also the flux of ions and back diffused electrons towards the cathode. In the sheath the number of collisions is insignificant and thus neglected. Therefore, there is no local thermodynamic equilibrium, no ionization and no recombination. The heat transferred to the cathode surface because of these charge fluxes includes

- the heat lost by thermal-field emission, by secondary emission, and radiative cooling.
- the heat gain by the ions and back diffusion electrons crossing the sheath and reaching the cathode surface.

These quantities depend on the cathode surface temperature, the electron and ion temperature at the sheath/pre-sheath interface, the plasma composition at the sheath/pre-sheath interface and the potential drop across the sheath.

2.4 Ionization zone (cathode pre-sheath)

The ionization zone is the region where charged species are produced by ionization. As sketched in Figure 2.6, the ionization can occur when an electron emitted from the cathode surface and accelerated in the sheath, collides with gas atoms or ions. The ionization can then take place if the kinetic energy of the electron is large enough so that an electron bound to the atom or ion overcomes the ionization threshold, resulting into two free electrons and a positively charged ion. The thickness of this layer is of the order of $10^{-5}m$ [56] which is less than the recombination length and much larger than the mean free path. The ionization layer is thus in partial local thermal equilibrium [12]. It means that electrons are in local thermal equilibrium and so are the heavy particles, but the electron temperature is much higher than the heavy particles temperature. The ionization layer is also quasi-neutral as the Debye length is less than the ionization mean free path. To summarize, the cathode layer presents three types of deviations from LTE [2]:

- Deviation from thermal equilibrium in the pre-sheath (see T(x) in Figure 2.7). This is the relative deviation of electron temperatures T_e from the heavy particle temperatures T_h.
- Deviation from ionization equilibrium in the pre-sheath, leading to a net production of charged particles that sustain the discharge ($\dot{n}_e \neq 0$).
- Deviation from quasi-neutrality in the sheath (see n(x) in Figure 2.7). This is due to the relative deviation of electron and ion densities, n_e and n_i.

The last deviation induces a significant potential drop (see V(x) in Figure 2.7) allowing the sheath to play its role for enhancing thermoionic emission.

	thermal equilibrium	ionization equilibrium	quasi neutrality
sheath	not defined	no ionization	$n_e \neq n_i$
pre-sheath	$T_e \neq T_h$	$\dot{n}_e \neq 0$	$n_e = n_i$
plasma core	$T_e \simeq T_h$	$\dot{n}_e = 0$	$n_e = n_i$

Table 2.1: Violation from L.T.E for plasma sub-regions.

Table (2.1) shows the summary of the plasma structure regarding the violation from LTE.

The anode layer is also divided into sheath and pre-sheath sub-regions. The distribution of the charged particles in the anode layer is different to the one in the cathode layer. However, plasma core-anode coupling obeys a similar concept

as plasma core-cathode coupling [6, 27, 36]. Therefore, the plasma core-anode coupling can be modelled as a plasma core-cathode with some modifications. This region is not further detailed here.

The cathode layer modelling can be applied if it is possible to do an energy coupling between the cathode and the plasma arc. Thus, before going into more details about the cathode layer modelling, a thermal coupling of solid-fluid is implemented in OpenFOAM. More details of this study can be found in [33]. The results obtained with this solid-fluid coupling are described in chapter 3.

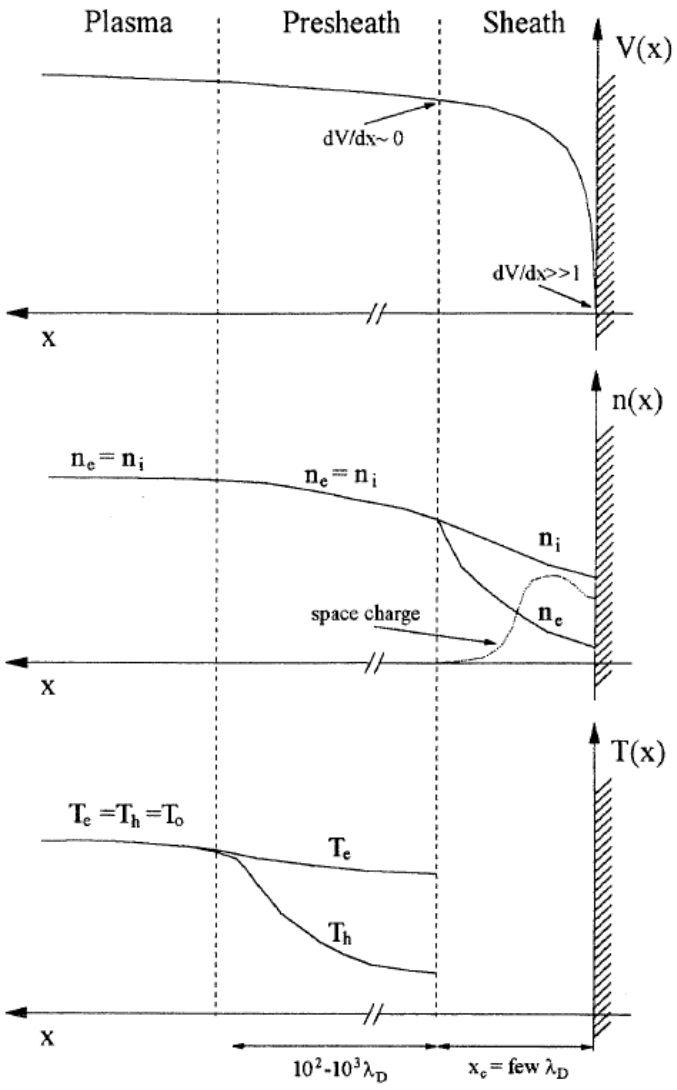

Figure 2.7: Schematic representation of the voltage V, particle number density n and temperature distribution T in the cathode region of a thermal arc emitting cathode [16].

Chapter 3

Solid-fluid coupling - summary of Paper A

A thermal solid-fluid model with a standard coupling is applied to a laser welding problem with shielding gas neglecting metal melting. The main reason for choosing a laser welding application is that it does not require any advanced model for coupling the shielding gas to the solid, contrary to arc welding. This application was also motivated by problems met in a manufacturing context: the smoke produced during welding could flow through the observation area of the optical system used to track the weld path, and thereby affect the accuracy of the path tracking. A better knowledge of the shielding gas flow was thus needed.

In this application a first argon shielding gas is brought by a pipe above the base metal around the focal point of the laser heat source. A second argon shielding gas is used to form an additional screen large enough to cover the part of the weld already solidified but not yet cooled. This second shielding gas is injected through a porous plate fixed on the back side of the pipe (see Figure 3.1).

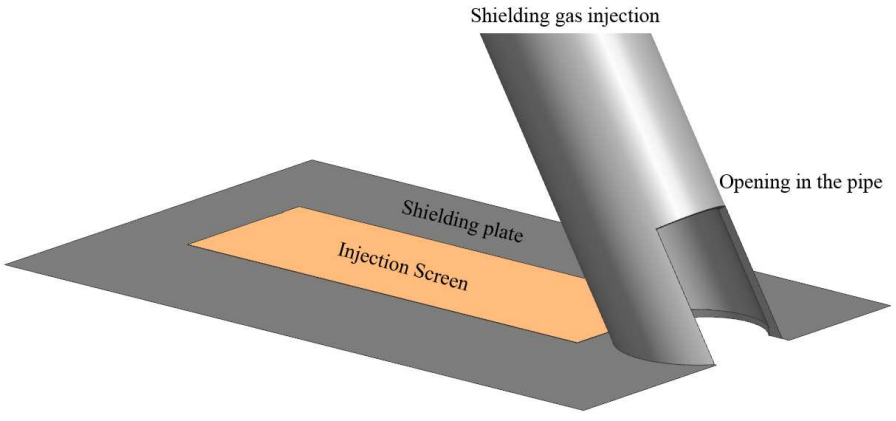

Figure 3.1: Schematic sketch of the shielding plate for case 4

The open source software OpenFOAM-1.6.x is employed to run the numerical calculations. The CFD tool OpenFOAM is a general library of C++ classes for numerical simulation of continuum mechanic problems, and it is mainly used in CFD. The solver so called chtMultiRegionFoam combining heat conduction in a solid region (the workpiece) and thermal flow in a fluid region (the shielding gas) is used. The domain plotted in Figure 3.2, is divided into two different parts: the solid part, and the fluid part. The solid domain is made of Ti6Al4V alloy and the fluid part contains pure argon gas. The fluid part contains the shielding pipe and in one case the shielding plate too.

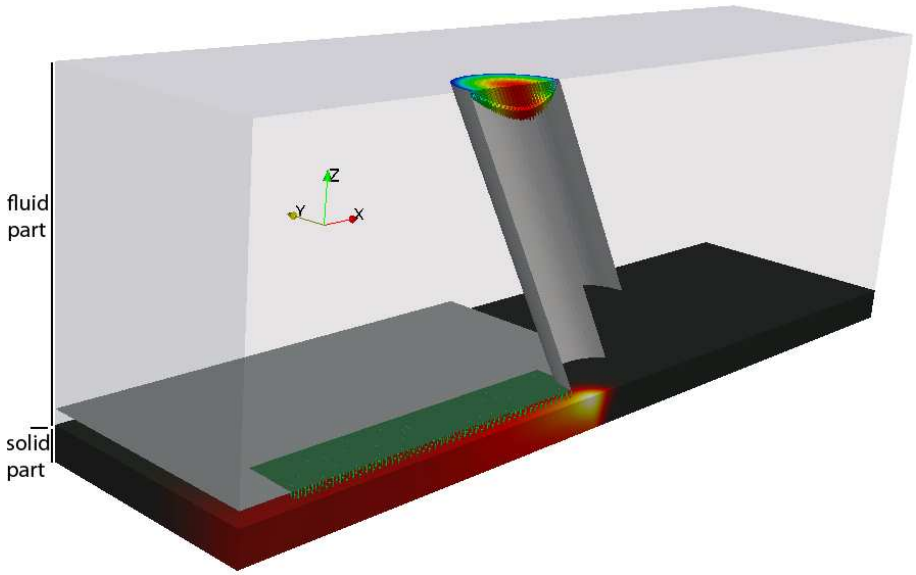

Figure 3.2: Schematic sketch of a section of the model

The model combines heat conduction in the solid region (the work piece) and thermal flow in the fluid region (occupied by the shielding gas). These two regions are coupled through their energy equations so as to allow heat transfer between solid and fluid region. The laser is modelled as a heat source acting locally on the surface of the work piece.

3.1 Governing equations

The simulations include both a fluid part and a solid part, where different governing equations are solved.

3.1.1 Governing equations in the fluid part

The system of equations governing the flow is the set of steady laminar Navier-Stokes equations for an incompressible and thermal fluid. This set is expressed in cartesian coordinates (x, y, z). In the sequel, x denotes the location along the welding direction, z along the direction through the solid and y is the location perpendicular to the two former (see Figure 3.2).

In this application the mass, momentum and enthalpy conservation equation are simplified versions of the LTE-plasma core equations: there is no Lorentz force, no Joule heating, no radiation cooling and no transport of electron enthalpy. The heat is generated in the solid part and transferred to the fluid through diffusion.

3.1.2 Governing equation in the solid part

A thermal energy equation is solved in the solid region. The governing heat conduction equation accounting for laser heating differs from the cathode equation: Joule heating is replaced by the heat source generated by the laser, and the equation in chtMultiRegionFoam solver is function of temperature rather than the enthalpy. It can be written as

$$U_i^r \frac{\partial}{\partial x_i}(\rho^s c_p^s T) - \frac{\partial}{\partial x_i}(K^s \frac{\partial T}{\partial x_i}) = Q_{ls} \tag{3.1}$$

where U_i^r is the i^{th} component of the relative velocity of the work piece with respect to the laser heat source. ρ^s is the solid density, c_p^s the specific heat at constant pressure, K^s the thermal conductivity of the solid material, and Q_{ls} the laser heat source. A guassian laser energy distribution is commonly used to model the laser heat source. In this study the volumetric laser heat source Q_{ls} is modelled according to Chuan et al. [15], i.e.

$$\begin{aligned} Q_{ls}(x, y, z) &= \frac{2\eta P^L}{\pi {r_e}^2 H} exp(\frac{-r^2}{r_0^2}), \\ r^2 &= x^2 + y^2, \\ r_0 &= r_i + \frac{(r_e - r_i)z}{H}, \end{aligned} \tag{3.2}$$

where η is the thermal efficiency, P^L the laser power and r_e and r_i are the half width of the weld at the top and bottom surface, respectively. In this study, which is concerned with full penetration laser welding, the welding penetration H is the thickness of the work piece, see Figure 3.3.

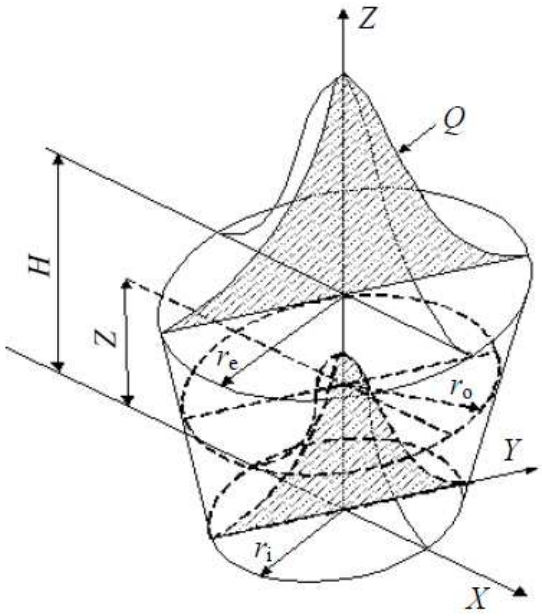

Figure 3.3: Heat source power density distribution [15]

3.2 Test cases and numerical settings

The parameters needed to set the test cases were taken from a manufacturing application. The thickness of the work piece is $7\,mm$, its length is $200\,mm$ and its half-width is $50\,mm$. A pipe with $20\,mm$ diameter is included in the model to inject argon with the flow rate of $45\ l/min$. The pipe makes a $60°$ angle with the horizontal line, see Figure 3.4.

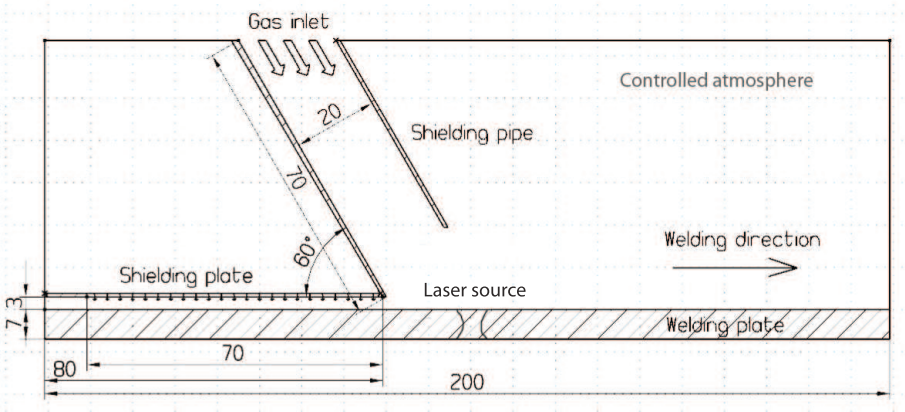

Figure 3.4: Partial cross section of the model [mm]

The velocity of the moving heat source is $800\,mm/min$. The heat source models a $TEM00$ laser with a power of $2500\,W$. A thermal efficiency of 100%

is considered and the width of the weld at top and bottom of the fusion zone are $7\,mm$ and $3\,mm$ respectively. The density, viscosity and thermal conductivity of the argon shielding gas are

$\rho^f = 0.686\ kg\ m^{-3}$,

$\mu = 0.432 \times 10^{-4}\ kg\ m^{-1}\ s^{-1}$,

$k^f = 0.0338\ W\ m^{-1}\ K^{-1}$.

The density, specific heat and thermal conductivity of the titanium alloy work piece are

$\rho^s = 4309\ kg\ m^{-3}$

$C_p^s = 714\ J\ kg^{-1}\ K^{-1}$,

$K^s = 17.8\ W\ m^{-1}\ K^{-1}$.

To study the shielding gas behaviour over the work piece, four different cases have been tested. Three cases aim at investigating the effect of the shielding pipe outlet shape on the gas flow without shielding plate, see Figure 3.5. These cases are done for pipes that are not equipped with a plate. The fourth case is inspecting the influence of the shielding plate on the gas flow, see Figure 3.1.

Case 1 includes the left pipe of Figure 3.5 and no shielding plate. This first pipe has an end opening normal to the pipe axis but no lateral opening. This configuration cannot be used in practice, as it would not allow the laser beam to reach the work piece. This test case was however studied since it gives information on the influence of the lateral opening of the pipe on the shielding gas flow.

As can be seen in Figure 3.5 the shielding pipe of case 2 is based on case 1 but with the presence of an additional opening on the wall of the pipe to let the laser beam reach the base metal (see Figure 3.5, centre). The dimension of the opening is $13\,mm \times 20\,mm$.

Case 3 differs from case 2 by the shape of the outlet of the pipe (see Figure 3.5, right). The angle between the pipe end opening and the pipe section is equal to 30° in the third case while it was equal to 0° in the former cases.

The model in case 4 is implemented with the same features as case 3, supplemented with a shielding plate. The shielding plate has an injection screen through which the gas flows at a rate of $45\ l/min$ to cover the welded part, see Figure 3.1. The injection screen of the shielding plate has a length of $70\,mm$ and an half-width of $20\,mm$. The geometry of the model is illustrated by the cross-section in Figure 3.4. The meshes of cases 1 to 3 have about 3.3 million cells. Case 4 has only about 1.4 million cells since the region located over the shielding plate and behind the pipe does not need to be included into the computational domain.

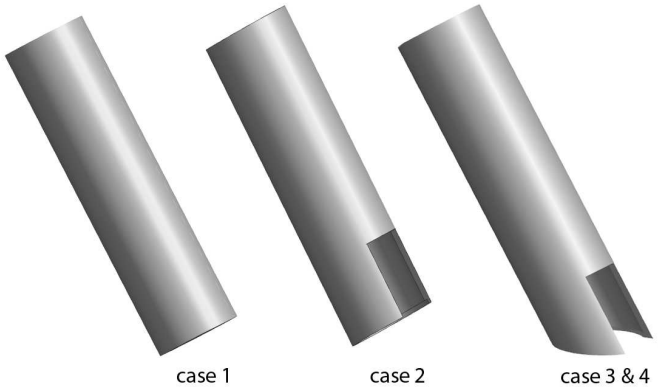

Figure 3.5: Shielding pipe for different cases

3.3 Boundary conditions

Boundary conditions are applied for the fluid part, the solid part, and the interface between them.

Fluid part

A parabolic velocity distribution is specified at the inlet of the shielding pipe. To achieve the flow rate of $45\ l/min$, a maximum velocity of $4.77\ m/s$ is employed. In case 4, where the shielding plate is included, an inlet boundary with uniform velocity of $1.9\,m/s$ is also set at the injection screen to form a shielding screen with a flow rate of $45\ l/min$. At the surrounding boundaries of the fluid part (on top and sides), a zero gradient condition is used for the velocity and the pressure is set to the atmospheric pressure. The inlet temperature of the shielding gas is at room condition, that is $300\ K$. The same temperature condition is applied to the fluid boundaries (on top and sides) of the computational domain. It was checked (running calculations with a larger computational domain) that the size of the computational domain is large enough to allow using such boundary conditions.

Solid part

In the manufacturing application, cooling water was flowing into a duct mounted under the work piece. The water inlet temperature was 6° C. The details of the cooling system were not included in the simulation model. The cooling effect was accounted for in a simplified way in the simulation test, assuming a fixed temperature condition $T = 300\,K$ at the bottom solid boundary. This value was calculated using standard analytic models for heat transfer in pipe flow. A zero gradient boundary condition is employed for the temperature at the sides of the solid part.

Interface between solid and fluid

At the interface between the solid and fluid regions, a common no-slip boundary condition is set for the fluid velocity. Solid and fluid are coupled through their energy equations so as to allow heat transfer between solid and fluid region. The energy equation in the solid region governs the solid temperature, while the energy equation in the fluid region governs the fluid enthalpy. So their coupling is not direct: the direction of the heat flux is first determined. Then, the thermal coupling is done setting automatically the fixed value or the fixed gradient depending on the direction of the heat flux. This boundary condition, called a conjugation boundary for heat flux and temperature, is implemented by the solver chtMultiRegionFoam.

3.4 Temperature distribution

Figure 3.6 represents the temperature distribution over the base metal and through the work piece in case 4. As the model does not yet account for phase change, the maximum temperature raises up to $2100\,K$ which is higher than the melting point of titanium alloy Ti6Al4V which is about $1900\,K$. The temperature distribution over the work piece along the x-axis is plotted for case 3 and case 4 in Figure 3.7. The x-axis is located at the intersection of the symmetry plane and the top surface of the solid region. It can be observed in Figure 3.7 that the weld temperature decreases strongly, by about $1300\ K$, over a short distance from the laser heat source ($40 < x < 90\ mm$). In this region, the cooling rates of case 3 and 4 are almost the same. The extension of the heat affected zone is less than $1/10^{th}$ of shielding screen area. So the volume flow rate of argon flowing effectively above the heat affected zone in case 4 is less than $4.5\ l/min$. A plot of the the velocity field in a cross-section under the shielding plate in $x = 50\ mm$ shows that above the weld (on the left hand side of Figure 3.8) the velocity of the shielding gas is very small. The shielding gas has thus in this region a poor ability to cool down by convective heat transfer. As a result, the presence of the shielding screen in this area does not improve the cooling.

Further away from the laser heat source (in $0 < x < 40\ mm$) the velocity of the shielding gas above the weld is slightly larger, see Figure 3.9 on the left. The cooling by convective heat transfer is thus slightly larger. Accordingly, in this region the solid surface temperature is almost $20K$ lower in case 4 than in case 3.

To conclude this part, the shielding plate does not provide any significant additional cooling of the weld. The shielding plate was indeed designed to protect the weld from the surrounding air, and not to further increase the cooling rate.

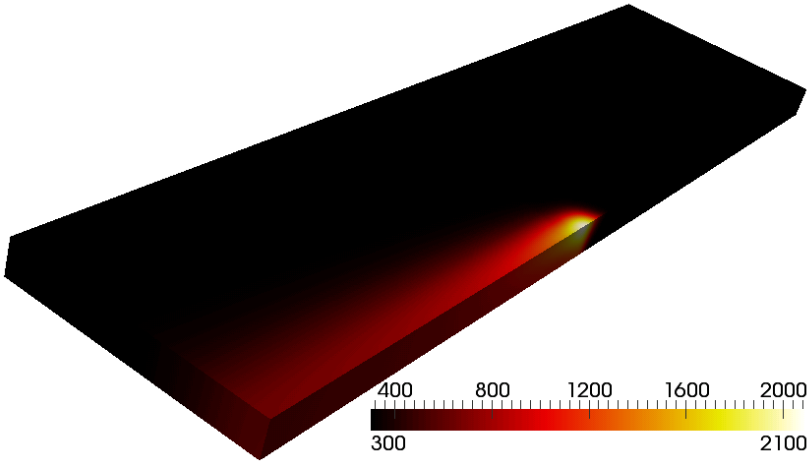

Figure 3.6: Temperature [K] distribution in the solid plate - case 4

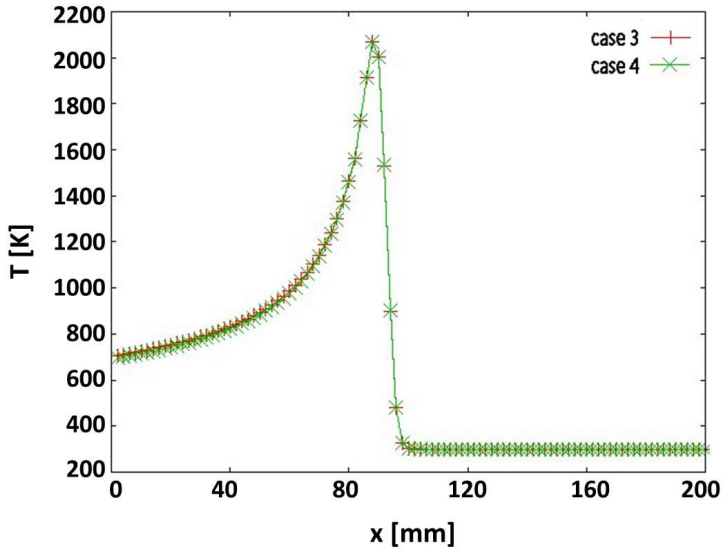

Figure 3.7: Temperature at the solid surface at the symmetry plane

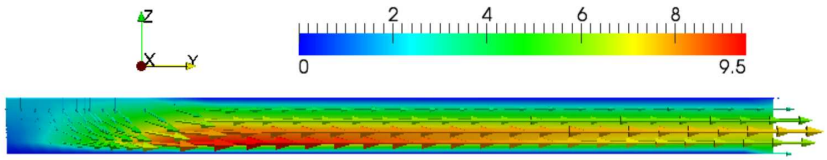

Figure 3.8: Velocity [m/s] in the cross section $x = 50\ mm$ of the shielding plate, case 4. The left hand side is at the symmetry plane. The right hand side is at the edge of the shielding plate.

3.5 Velocity distribution

To compare the results obtained with the different test cases, the magnitude of the velocity is plotted in the symmetry plane.

Comparing Figures 3.10 top and bottom reveals that the velocity profile and magnitude in case 1 and case 2 have almost the same patterns and values. The argon gas injected in the pipe is not pressurized. Pressure gradients along the radial direction from pipe axis to the surroundings are thus negligible at some distance above the work piece. Closer to the work piece the argon pipe jet is deflected because of the presence of the base material surface. As the pipe end opening and the work piece make an angle of $30°$, the open space is large enough for the argon jet to be deflected without disturbing significantly the flow inside the pipe and thus in the lateral pipe opening. So, with the configuration of case 2, the opening on the pipe wall does not affect significantly the shielding gas distribution compared to case 1. Increasing enough the volume flow rate of the shielding gas, or reducing enough the angle between the pipe end opening and the work piece, would change this result.

The magnitude of the velocity obtained with the test case 3 is plotted in Figure 3.11. Figure 3.11 shows that when reducing the angle between the pipe end opening and the work piece down to $0°$, the shielding gas flow behaves differently and a higher velocity is achieved over the base metal. So this pipe configuration is less favourable than the configuration of case 2, since a higher shielding gas velocity towards the front of the weld will most probably entrain more smoke in the observation area of the optical system intended to track the welding path.

The velocity fields of case 4, plotted in Figure 3.8 and Figure 3.9, confirm that the protection against the oxidizing surrounding atmosphere is achieved by the shielding screen since the shielding gas prevents the atmosphere from flowing towards the weld.

Figure 3.12 is a zoom at the junction between pipe and shielding plate, showing the velocity vectors of the shielding gas in the symmetry plane. It indicates that part of the shielding screen (from the plate) flows towards the pipe, joins the pipe flow and thus increases the amount of gas flowing towards the front of the weld. This flow can entrain even more smokes and fumes towards the front of the weld and the observation area of the optical system.

3.6 Conclusions

The flow of the laser welding shielding gas over the base metal with both shielding pipe and shielding plate has been studied. The present results confirm that the shielding plate provides a good protection of the cooling weld against the surrounding atmosphere. The shielding screen produced by the plate has a neg-

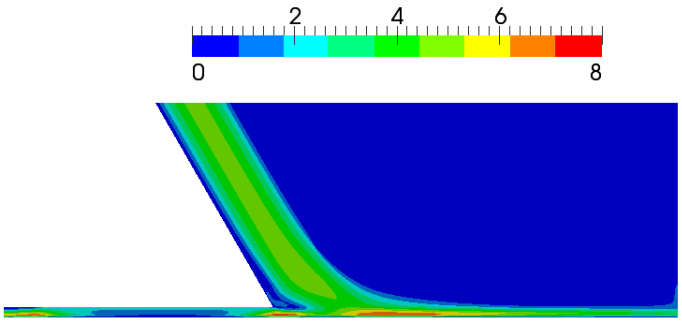

Figure 3.9: Velocity [m/s] at the symmetry plane case 4.

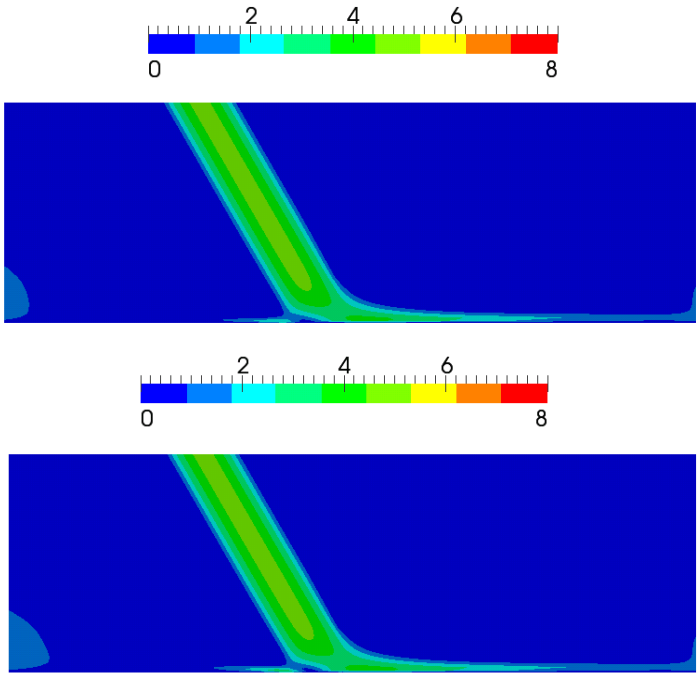

Figure 3.10: Velocity [m/s] at the symmetry plane. Top: case 1, bottom: case 2

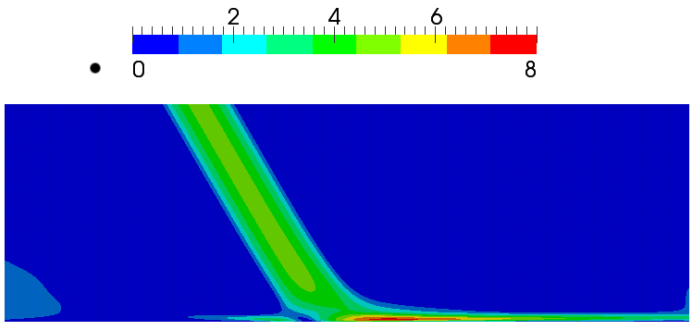

Figure 3.11: Velocity [m/s] at the symmetry plane case 3

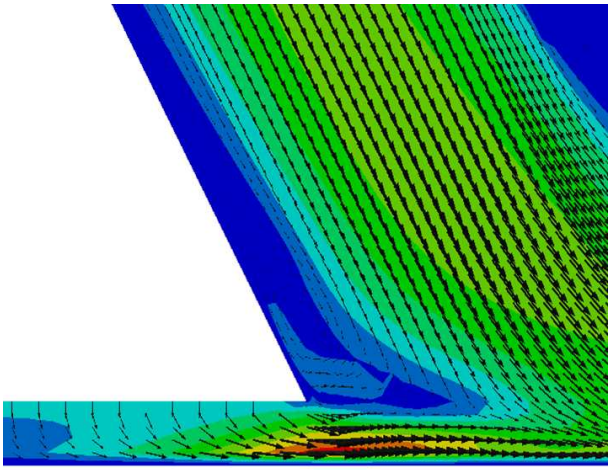

Figure 3.12: Zoom of case 4 showing the velocity vectors in the symmetry plane, at the junction between pipe and shielding plate.

ligible influence on the cooling rate of the weld. However, the design of the shielding pipe and plate (case 4, the case used in practice) is in conflict with the requirements of the optical system for tracking the welding path. A larger angle between end pipe opening and work piece, as in case 2, leads to lower shielding gas velocity towards the front of the weld compared to case 3 (and 4), but this is not sufficient to protect the observation area from the possible entrainment of fumes by the shielding gas. Based on case 2, more extended lateral openings on the pipe wall are not expected to provide any significant improvement. The design of the pipe and plate should thus be modified to deflect differently the shielding gas flow, away from the observation area, while maintaining a proper shielding. A solution could be to force a lateral flow of the shielding gas by introducing pressure gradients. Checking with CFD that a new design is suited will require a more detailed modelling of the flow, accounting for turbulence, as the pipe flow is known to be transient (see section 2), and turbulence may also disturb the observation area of the optical system for tracking the welding path.

The extension of the OpenFOAM solver chtMultiRegionFoam to a welding arc model coupling the plasma arc heat source with the electrode and base metal requires first implementing a coupled electromagnetic model for the solid and fluid region. This technical part is not detailed here and can be found in the report [32]. The second step concerns the modelling of the interface layer coupling the arc core and the solid acting as electron emitter. This model is presented in the next chapter.

Chapter 4

Cathode layer

4.1 Problem description

The problem raised by cathode layer modelling is the following: two regions (see Figures 2.6 and 2.7)

1. plasma core and pre-sheath,
2. cathode bulk

can be modelled at the macroscopic scale. These regions are separated by a third region the sheath, in which the macroscopic approach is not valid. However, because of the physics taking place in the sheath, the heat $q_{ps/s}$ transferred from the pre-sheath region is not equal to the heat q_{cath} transferred to the cathode bulk (see Figure 4.1).

With a multi-species (electrons, ions, atoms) and multi-temperature (T_e, T_h) fluid model for thermal arc with ionization non-equilibrium, it would be possible to model the plasma core and the pre-sheath together (see Figure 4.1). The heat $q_{ps/s}$ transferred from the pre-sheath towards the sheath could then be known based on the fluid model. Then the cathode layer model would reduce to a sheath model for finding the potential drop across the sheath, and the heat transferred from the sheath to the cathode surface q_{cath}.

Several multi-fluid and two-temperature models do exist in the literature for modelling a thermal arc. They were recently compared by Freton et al. [20]. These models differ in the way the energy source terms for heavy and light particles are handled. A problem is that most of these models do not account for the ionization non-equilibrium needed for the pre-sheath. Multi-temperature and non-equilibrium ionization model involve a large number of PDE to be solved throughout the arc, thus high computational cost.

As most of the thermal arc core is in LTE, it could be more interesting to opt for a one fluid LTE model describing the arc core alone. The heat $q_{p/ps}$

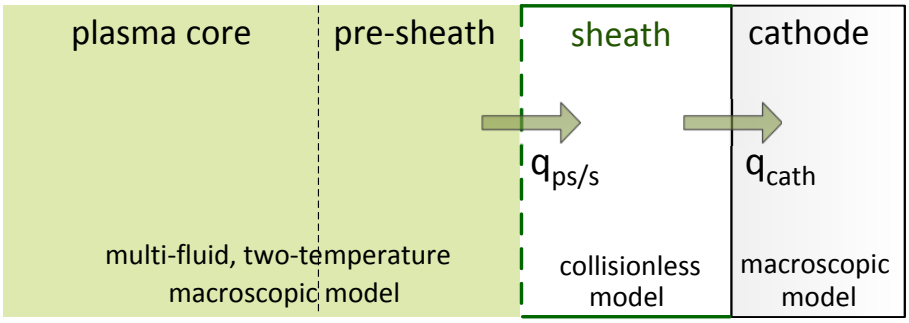

Figure 4.1: Scheme of sub-regions of an arc discharge with multi-fluid, two-temperature fluid model.

transferred from the plasma to the pre-sheath (see Figure 4.2) can be known based on the LTE-fluid model. Then cathode layer model must include both the pre-sheath and the sheath for finding the conditions at the pre-sheath/sheath interface so as to determine the potential drop across the sheath, and the heat transferred from the sheath to the cathode surface q_{cath} (see Figure 4.2). As a counterpart, additional closure relations are needed for finding electron and ion temperature as well as plasma composition at the pre-sheath/sheath interface. This is the approach retained in this study.

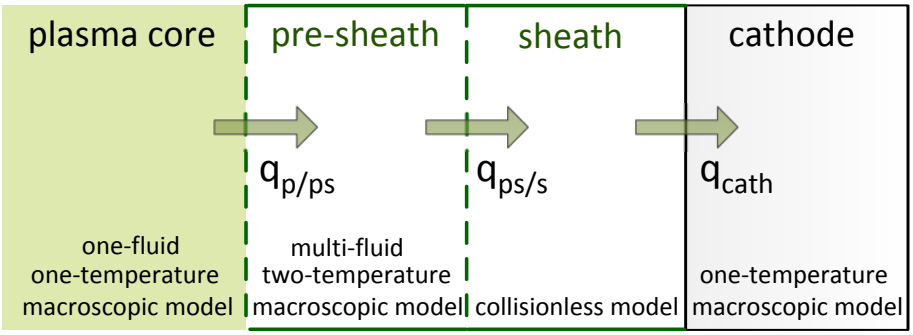

Figure 4.2: Scheme of sub-regions of an arc discharge with one-fluid, one-temperature fluid model.

4.2 Existing models

The literature addressing this problem can be divided into two different groups. The first group focuses on the physics of the cathode layer without considering a fluid model (the arc is modelled setting LTE boundary conditions). Lowke [38], Hsu and Pfender [31], Zhou and Heberlein [58, 59], Schmitz and Rieman

[49, 50] and Benilov and Marotta [5] did successively contribute to cathode layer modelling. Some main characteristic of their models are now summarized.

Lowke's theory [38] treats the pre-sheath as a one-temperature region and does not take into account the sheath. In this way, the electron density close to the cathode is larger than the electron density of a LTE plasma. This thus promotes the current flow from the cathode to the plasma. This phenomenon of electron enrichment is equivalent to considering a chemical non-equilibrium within the ionization layer. Thanks to the calculation of the electron density distribution in the cathode vicinity, the electric conductivity can be calculated. As a result the current flow between the cathode and the plasma is ensured in a self-consistent way. The main drawback of this model is to ignore the space charge layer and to present inconsistencies in the determination of current densities.

Zhou and Heberlein [58, 59] do not take into account the physical concepts of the ionization layer. However, they calculate the plasma composition at the sheath/pre-sheath interface thanks to a two-temperature composition model. Two other important features of this model are to include the back diffusion electron current and to consider a heavy particle temperature at the sheath/pre-sheath interface equal to the cathode surface temperature. The main drawback of this model is that it requires setting several parameters like cathode voltage drop, cathode spot radius and electron temperature.

Hsu and Pfender [31] consider the sheath as a collisionless domain and solve a Poisson equation which satisfies charge conservation. The ionization layer in their model is described using a two-temperature model. They consider two conservation equations for the charge and two conservation equations for the energy. They use the current density at the cathode surface as input parameter for the cathode layer model. This aspect is important when planing coupling this cathode layer model with the cathode bulk and plasma core. The main drawback of this model is that the two-temperature model involves an invalid Saha equation.

Schmitz and Rieman [49, 50] divide the pre-sheath layer into two sub-regions: (1) the transition zone where the ionization takes place. Within this sub-region the charge densities are calculated. (2) The Knudsen zone in which collisions can take place without ionization. The Knudsen zone can be described by the Boltzmann equation. The problem with this model is that the detailed description of the ionization layer makes it difficult to be used for other gases. Nandelstädt et al. [40] showed that the results of this model are close to the results by Benilov while the the Benilov's model is not as complex as the Schmitz model.

The work by Benilov and Marotta [5] is the most fundamental of the models within the frame of this approach. In their model the energy balance equations at the cathode/sheath interface and also in the pre-sheath are considered. Theses energy balances are implemented by introducing electron emission heat flux,

electron back diffusion heat flux and ion heat flux. The calculation of these heat fluxes gives the current density in the space charge layer and the energy flux towards the cathode. In the ionization layer the electrons, ions and neutral atoms are considered as different fluids while treated with a two-temperature model. The ion density at the sheath edge is calculated based on the ion density of a LTE-plasma core. The surface electric field is used to calculate the Schottky correction in the Richardson emission formula to account for the field enhancement of the thermoionic emission from the cathode surface. A drawback of this model is that it does not consider secondary emission, and the current and energy conservation at the sheath/pre-sheath interface are not strictly verified. The main novelty and drawbacks of each study are summarized in Table 4.1.

The second group of modelling studies is more recent, and contrary to the former group, often related to electric arc welding applications. In this group the arc plasma described by magnetohydrodynamic equations is part the model. The aim of this group of models is indeed to supplement the arc plasma model with the electrodes. Studies in the frame of this group can be classified into two different approaches.

In the first approach, the thermal arc is described with a multi-species (electrons, ions, atoms), two-temperature (T_e, T_h) and chemical non-equilibrium fluid model. So the fluid model for the arc is also valid for the ionization layer. There is thus no need to model the pre-sheath and the cathode layer model reduces to a sheath model. Consequently, the thermal-field emission electron flow, secondary emission electron flow, the ion flow, and the back diffusion electron flow taking place in the sheath need to be taken into account to calculate the voltage drop in the sheath (U_s) and the heat (q_{cath}) transferred to the cathode surface. A problem is that different models do exist in the literature for modelling a thermal arc in the frame of this approach (e.g. Haidar [28] and Tashiro [52]). As underlined earlier, they differ in the way the energy source terms for heavy and light particles are handled and are based on a phase composition models that are not satisfying yet. In addition, Haidar [28] and Tashiro [52] do not account for the enhancement of thermoionic emission by the sheath electric field, nor the back diffusion electrons and the secondary emission. Also, Haidar [28] and Tashiro [52] do not take into account the charge particle acceleration in the sheath because they do not calculate the voltage drop in this region. In the studies by Haidar [28] and Tashiro [52], the emitted electrons and ions flowing backwards to the cathode are the only current densities considered, besides the current density is not conserved in their model.

In the second approach the thermal arc is modelled as a LTE fluid considering a one-fluid, one-temperature model and chemical equilibrium. In this approach, the fluid model is not valid for the ionization layer. This last region thus need to be included in the cathode layer mode. The models of this approach are built

	Novelty	Drawbacks
Lowke	• The electric conductivity in the cathode vicinity accounts for physical properties of the cathode layer. • The current density at the cathode surface is used as input parameter for the cathode layer model.	• Inconsistencies in the current density expressions in the cathode layer. • Does not describe the space charge layer.
Zhou and Heberlein	• Considers electron back diffusion density. • Considers the heavy particle temperature equal to the cathode surface temperature.	• Several parameters should be set.
Hsu and Pfender	• Considers two temperature model to describe the sheath • The current density at the cathode surface is used as input parameter for the cathode layer model. • The back-diffusion electron flux is taken into account.	• The transport coefficients are calculated using an invalid equation [42]. • Tested only for a high value of the current density (larger than $108 A.m^{-2}$).
Schmitz and Rieman	• Introduces the Knudsen layer at the sheath/pre-sheath interface.	• Difficult to extend to other gases. • The results are close to results of simpler model by Benilov [40]. Thus, the complexity seems to be useless.
Benilov and Marotta	• Easy to extend to other gases. • Experimentally validated [40]. • Takes into account back diffusion electron density.	• Does not consider secondary emission.

Table 4.1: Novelty and drawbacks of the models in the frame of level-1 (based on [9]).

on the studies done in group-1 based on the physics of the cathode layer alone. Cayla [8, 9] did developments starting from Benilovs studies [1, 2, 3, 4, 5]. Some of the main improvements proposed by Cayla et al. are as follows:

- The pre-exponential factor of the equation for electron emission current density is modified to be generalized independently from the material properties, (see equation (5.2)).
- The charge density at the sheath/pre-sheath interface is determined using the Saha equations consistent with thermodynamic and kinetic law, developed by Van de Sanden et al. [54], (see equation (5.20)).
- The second electron emission is taken into account (see equation (5.16)) and shown to be significant for low cathode surface temperature ($T < 2700K$). This is important in GTAW applications as the cathode surface temperature is less than the material melting temperature, and the melting temperature of tungsten is about $3700K$.
- The heat conduction towards the cathode bulk (calculated solving a conduction equation in the solid cathode) is added to the energy balance equation at the cathode/sheath interface, (see equations (5.25), and (5.26)).

A drawback of this model is that the current and energy conservation at the sheath/pre-sheath interface are not strictly verified.

The aim of the present work is to further improve the model developed by Cayla, and prepare a numerical model of cathode layer which can be applied to welding applications. The cathode layer model is described in the next chapter.

Chapter 5

Cathode layer - model

This chapter focuses on the modelling of the cathode layer assuming that the plasma core can be described by a one-fluid model at LTE. It then requires modelling both the cathode sheath and the pre-sheath in order to determine

- the net heat flux towards the cathode surface, q_{cath}, and
- the net charge flux from the cathode surface, J_{cath}.

These two quantities do allow coupling energy and charge (or current) conservation equations between plasma core and cathode.

To be able to do such a calculation, the analysis of the current densities from and to the cathode surface is needed. This is described in section 5.1. To calculate the current densities coming from the pre-sheath, the electron and heavy particle densities $n_e, n_{Ar}^j (j = 0, ..., 3)$ and the temperatures T_e, T_h, are needed at the sheath/pre-sheath interface. As they cannot be provided by the one fluid model at LTE, they are calculated from closure relations inferred from physical concepts. The first step consist in calculating the plasma composition. This is done solving the Saha equations (function of T_e), closed with the Dalton equation for pressure and the charge neutrality equation. The electron temperature is obtained from the energy conservation in the sheath. All these elements needed for calculating T_e, T_h, n_e and $n_{Ar}^j (j = 0, ..., 3)$ at the sheath/pre-sheath interface are described in section 5.2 and 5.3.

Finally the cathode surface temperature T_c as well as the sheath voltage drop are also needed to calculate the flux of electrons emitted by the cathode surface (and the charged particle acceleration across the sheath). The physical concepts allowing establishing the needed closure relations are energy and charge conservation at the sheath/cathode interface. These relations are described in sections 5.3.1 and 5.3.3. The calculation and numerical procedure allowing solving this large system of coupled equations are presented in sections 5.4 and 5.5.

5.1 Current densities in the cathode layer

Developing the current densities is essential for calculating the heat fluxes and the energy balance equations at both the cathode/sheath boundary and the sheath/pre-sheath interface. As discussed in chapter 2, there are four main charge fluxes at

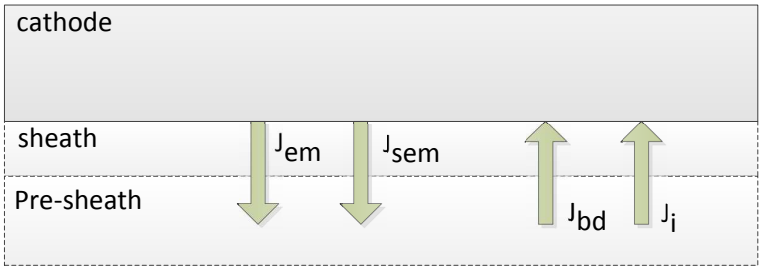

Figure 5.1: Current densities at the cathode layer

the cathode surface (see Figure 5.1) which make the total current density, or cathode current density

$$J_{tot} = Z J_i + J_{em} + J_{sem} - J_{bd}, \tag{5.1}$$

where J_i denotes the positive ion current towards the cathode, J_{em} the thermal-field electron emission from the cathode, J_{sem} the secondary emission current density from the cathode and J_{bd} is the electron back diffusion current density towards the cathode. These current densities are now presented in more details.

1. **Thermal-field emission current density**
   Conducting metals use to have one or two valence electrons per atom that are free to move between atoms. The minimum energy that must be given to a metal surface to liberate an electron is the work function (see section 2.2). By absorption of sufficient thermal energy, a metal surface can emit electrons by thermoionic emission. The thermal energy is provided by the ions colliding with the surface. The thermoionic electron emission current density is calculated by Richardson emission formula [17]

   $$J_{em} = A_R \, T_c^2 \, \exp\left(-\frac{\phi_{eff}}{k \, T_c}\right), \tag{5.2}$$

   where k is the Boltzman constant, T_c the cathode surface temperature and $A_R = 4\pi k^2 m_e / h^3 = 1.2 \times 10^6 \;\; A.m^{-2}.K^{-2}$ is the Richardson constant. ϕ_{eff} is the effective work function. For pure thermoionic emission ϕ_{eff} is the work function ϕ. When the thermoionic emission is enhanced by the potential drop in the space charge layer, ϕ_{eff} also accounts for Schottky correction which basically express the influence of surface electric field on

electron emission. It indicates that surface electric fields induce a lowering of the work function, allowing easier thermoionic emission of electrons

$$\phi_{eff} = \phi - \sqrt{\frac{e^3\, E_c}{4\pi\epsilon_o}}, \tag{5.3}$$

where ϵ_0 is the electric permittivity in vacuum, e is the electron charge and E_c is the surface electric field.

The electric field in the sheath derives from the electrostatic potential φ produced by the sheath space charge. It can be derived from a one-dimensional and steady state approach if the plasma parameters across the sheath vary much faster than in the transverse direction. This simplification is justified for usual welding arcs as their sheath thickness uses to be much smaller than the characteristic conducting cathode length (or cathode spot diameter). φ can thus be obtained solving locally the 1-dimensional Poisson equation,

$$\varepsilon_0 \frac{d^2\varphi}{dy^2} = e(n_e - Zn_i), \tag{5.4}$$

where y is the direction normal to the cathode wall surface oriented from the wall towards the plasma (see Figure 2.6), and n_e and n_i are the electron and ion number densities in the space charge layer. It can be noticed that the electrostatic potential φ is equal to zero at the sheath/pre-sheath interface because of local electro-neutrality in the pre-sheath.

To solve the Poisson equation (5.4) the electron and ion charge density in the space charge layer n_e and n_i need first to be determined. The sheath is collisionless for both ions and electrons as its thickness is less than the ion and electron mean free path. The ion and electron distribution functions are thus governed by collisionless Boltzmann equations. For charged particles accelerated by an electric field along the y-direction, the steady and collisionless Boltzmann equation governing the distribution function $f = f(y, v_y)$ (with $f = f_i$ for ions and $f = f_e$ for electrons) writes

$$v_y \frac{\partial f}{\partial y} - \frac{q}{m}\frac{d\varphi}{dy}\frac{\partial f}{\partial v_y} = 0 \tag{5.5}$$

where v_y is the particle velocity along y, q the particle charge ($q = e$ for electrons and eZ for ions), and m the particle mass ($m = m_e$ for electrons and m_i for ions). When the solution $f = f_e$ (resp. $f = f_i$) of equation (5.5) is known, the electron (resp. ion) charge density along y is

$$n = n_{e(i)}(y) = \int_{-\infty}^{B_e(i)} f_{e(i)} dv_y \tag{5.6}$$

The upper limit of integration B_e for electrons and B_i for ions is set below.

The ions present in the space charge layer come from the ionization layer while the electrons include both the back-diffusion electrons coming from the ionization layer and the emitted electrons coming from the cathode surface. However, as proposed by Benilov [5], this last contribution can be neglected since it is of the order $\sqrt{m_e/m_i}$ lower. The ion and electron distribution functions within the pre-sheath are Maxwellians at temperature T_i and T_e, respectively. The sheath electric field decelerates the back-diffusion electrons as they move toward the cathode, while it accelerates the positively charged ions. As a result, a large fraction of the back-diffusion electrons are reflected by the sheath potential barrier before reaching the cathode wall (and return to the pre-sheath) while the ions are accelerated up to collision with the cathode wall. It implies that the electron distribution function in the sheath can be assumed nearly isotropic in velocity, and approximated by a Maxwellian. It also implies that for electrons the upper limit of integration in equation (5.5) is $B_e = +\infty$. The ions reach the cathode surface and are all assumed to recombine. As they do not travel back towards the pre-sheath (neutral atoms do instead), their sheath distribution function is highly non-isotropic in velocity and cannot be assumed Maxwellian [39]. It also implies that for ions the upper limit of integration in equation (5.6) is $B_i = 0$.

In the space charge layer, the electron distribution function f_e is assumed to be Maxwellian. The electron density in this region can then be calculated from the first moment of the Boltzmann equation (5.5).

$$n_e = n_e(y) = n_{es} \exp(\frac{e\varphi}{kT_e}) \tag{5.7}$$

where n_{es} is the electron number density at the sheath edge. The ion density is more difficult to calculate as the ion distribution function f_i in the sheath is not known. The Boltzmann equation then needs to be solved. This requires knowing the boundary condition at the sheath/pre-sheath interface, $f_i(\infty, v_y)$.

Riemann [46] showed that smooth matching of the pre-sheath and sheath solution f_i requires an additional transition layer called the Knudsen region. The Knudsen region is a thin sub-region of the pre-sheath next to the sheath and dominated by ion-ion collisions with no ionization [5]. The role of this sub-layer is to transform the ion distribution function from a Maxwellian function on the pre-sheath side to a distribution of forward-going particles on the sheath side. According to our knowledge, there is no known solution of the Knudsen layer model when ion-ion collisions

are dominant. The following expression suggested by Benilov [5] is thus used:

$$f(\infty, v_y) = \begin{cases} \dfrac{n_{is}}{2u_i} & if \quad -(v_s - u_i) > v_y > -(v_s + u_i) \\ 0 & otherwise \end{cases} \tag{5.8}$$

where n_{is} is the ion number density at the sheath edge, v_s the absolute value of the mean velocity of the ions at the sheath edge, u_i the thermal velocity of the ions at the sheath edge,

$$u_i = \sqrt{\frac{kT_i}{m_i}} \tag{5.9}$$

k is Boltzmann constant, and T_i the ion temperature at the sheath edge.

It should be noticed that $Zn_{is} = n_{es}$ since the pre-sheath satisfies local electro-neutrality. The above expression for $f_i(\infty, v_y)$ reproduces the effect of the Knudsen layer in the sense that the velocity distribution of the ions leaving the ionization layer through the ion Knudsen layer and entering the space charge layer describes forward-going ions. The lower and upper velocity bound $v_s - u_i$ and $v_s + u_i$ result from Bohm's criterion. As explained by Riemann [46], "Bohm's criterion expresses a necessary condition for the formation of a stationary sheath in front of a negative absorbing wall". v_s is specified later on. The change of variable v_y to $1/2m_i v_y^2 + Ze\varphi$ allows obtaining the following ion distribution function $f_i(y, v_y)$ solution of equation (5.5) [5]

$$f_i(y, v_y) = \begin{cases} \dfrac{n_{is}}{2u_i} & if \quad -v_- > v_y > -v_+ \\ 0 & otherwise \end{cases} \tag{5.10}$$

where the maximal and minimal velocity at a given location in the space charge layer v_+ and v_- are

$$v_\pm = \sqrt{(v_s \pm u_i)^2 + \frac{2ZeU_s}{m_i}}, \tag{5.11}$$

as when considering mechanical energy conservation for particles falling freely into an electric field. The ion density in the space charge layer can then be calculated from equation (5.6), leading to

$$n_i = n_{is} \frac{v_+ - v_-}{2u_i}. \tag{5.12}$$

After substitution of n_e and n_i using the relations (5.7) and (5.11) in the 1-dimensional Poisson equation (5.4) and integration, the electric field in

the sheath is now obtained

$$E = \left\{ \frac{2n_i}{\epsilon_0} \left[m_i \left(\frac{v_+^3 - v_-^3}{6u_i} - v_s^2 - \frac{u_i^2}{3} \right) - ZkT_e \left(1 - \exp(\frac{-e\varphi}{kT_e}) \right) \right] \right\}^{\frac{1}{2}} \tag{5.13}$$

The absolute value of the mean velocity of the ions at the sheath edge v_s can now be expressed from equation (5.13) at the sheath/pre-sheath edge where local electro-neutrality must be satisfied. It implies that when φ tends to zero in equation (5.13), the velocity v_s is equal to the Bohm velocity [46]

$$v_s = \sqrt{\frac{k(T_c + ZT_e)}{m_i}} \tag{5.14}$$

The Bohm velocity represents the minimum ion velocity allowing forming the sheath (Bohm's criteria).

Finally, the electric field at the cathode surface E_c allows calculating the Schottky correction in equation (5.3). It can be expressed setting φ to the fall voltage U_s in the space charge layer, so that $E_c = E(-U_s)$

$$E_c = \left\{ \frac{2n_i}{\epsilon_0} \left[m_i \left(\frac{v_+^3 - v_-^3}{6u_i} - v_s^2 - \frac{u_i^2}{3} \right) - ZkT_e \left(1 - \exp(\frac{-eU_s}{kT_e}) \right) \right] \right\}^{\frac{1}{2}} \tag{5.15}$$

2. **Secondary emission current density**
When an ion colliding with the surface, brings to the surface an energy larger than the work function, it can directly induce the emission of an electron. This is called secondary emission (the primary emission is here the thermal-field emission).

In the study by Lichtenberg et al. [37] the secondary emission current density J_{sem} is proportional to J_i ($J_{sem} = \gamma J_i$) while in the work by Cayla et al. [9] for the argon plasma it is simplified to $J_{sem} = \gamma n_{Ar^+} v_s$. According to our investigation the value of J_{sem} calculated by those two approaches are the same for argon plasma. However, this may not be valid for other types of plasma. Therefore, in this study secondary emission current density is calculated according to equation (5.16) [37],

$$J_{sem} = \gamma J_i = \gamma n_i v_s, \tag{5.16}$$

where γ is the coefficient of secondary emission which depends on the plasma and electrode parameters. This coefficient is estimated to be equal to 0.1 for argon plasma and tungsten cathode [41]. J_i is the the ion current density.

In most of the studies [5, 56, 58] the secondary emission is not considered or assumed negligible. However, Cayla et al. [8] showed that J_{sem} cannot be neglected especially for the total current density commonly used in welding applications which is lower than $5 \times 10^6 A.m^{-2}$. The total heat flux to the cathode with and without secondary emission are compared in Figure (5.2), by Cayla et al. [9]. The value $\gamma = 0$ represents the case where the secondary emission is not considered.

Secondary emission causes the reduction of the heat flux to the cathode at low current density. The cathode surface temperature is then also significantly different as shown in Figure (5.3).

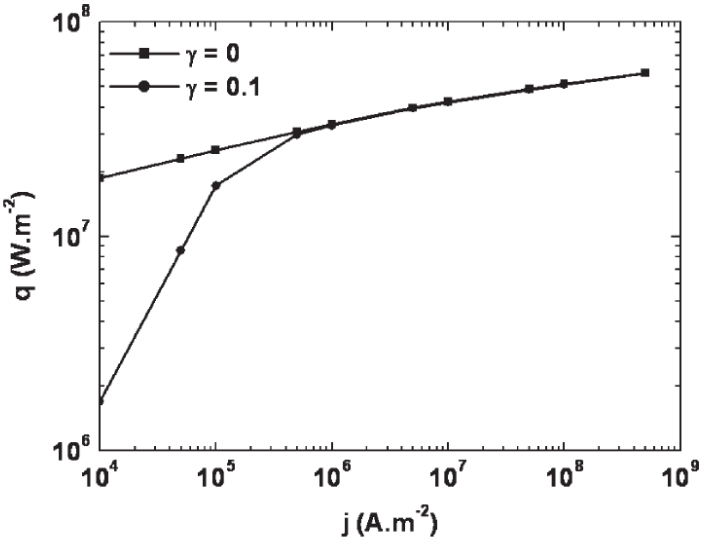

Figure 5.2: Total heat flux to the cathode versus total current density, done by Cayla et al. [9]

3. **Ion current density:**
   The ions resulting from ionization in the ionization layer (pre-sheath) produce the ion current density towards the cathode. To calculate this current density equation (5.17) is used.

$$J_i = n_i v_s, \tag{5.17}$$

where n_i is the ion number density and v_s Bohm velocity. The Bohm velocity refers to the minimum velocity allowing ion to enter the sheath region.

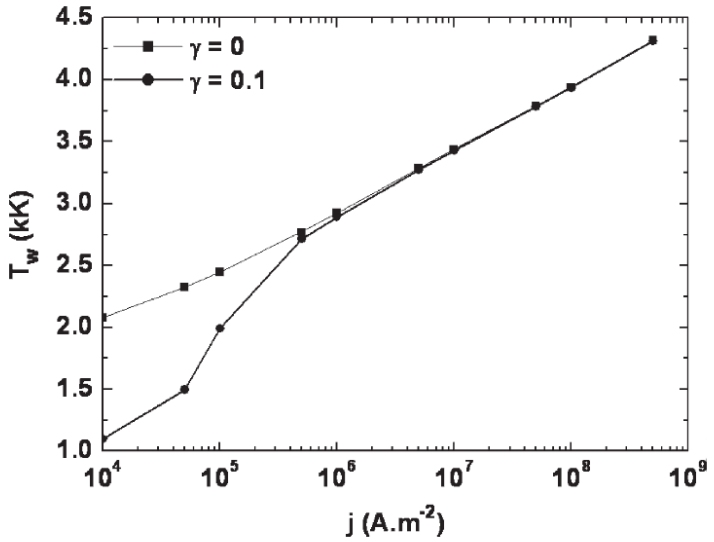

Figure 5.3: Cathode surface temperature versus total current density, done by Cayla et al. [9]

4. **Back diffusion current density:**
   The back diffusion current density is caused by electrons from the ionization layer moving in the sheath towards the cathode. As discussed in the previous sub-section on "Thermal-field emission current density", the distribution function of these electrons inside the sheath is Maxwellian, so

$$f_e(y, v_x, v_y, v_z) = n_{es} \left(\frac{m_e}{2\pi k T_e} \right)^{3/2} \exp\left(\frac{-m_e(v_x^2 + v_y^2 + v_z^2)}{2kT_e} \right) \quad (5.18)$$

   where the y-direction is normal to the cathode surface, and oriented towards the surface and n_{es} is the sheath electron density. For back diffusion electrons, the sheath potential is repulsive. Only fast plasma electrons ($v_y \leq -\sqrt{2eU_s/m_e}$) can overcome this barrier. As the back diffusion electrons are involved in ion recombination at the cathode surface the flux of electrons to the cathode surface is thus

$$\begin{aligned} J_{bd} &= \int_{v_x=-\infty}^{v_x=+\infty} \int_{v_y=-\infty}^{v_y=-\sqrt{2eU_s/m_e}} \int_{v_z=0}^{v_z=+\infty} v_y f_e(y, v_x, v_y, v_z) dv_x dv_y dv_z \\ &= \frac{n_{es} u_e}{\sqrt{2\pi}} \exp\left(-\frac{eU_s}{k\,T_e} \right), \end{aligned} \quad (5.19)$$

   with the electron thermal velocity $u_e = \sqrt{\frac{kT_e}{2m_e}}$.

The calculation of the electron density n_e, ion density n_i and argon ions densities at the sheath/pre-sheath interface are described in section (5.2).

5.2 Number densities at the sheath/pre-sheath interface

Two ionization processes can take place in thermal plasma: impact ionization and radiative ionization. The former, dominant at atmospheric pressure, is the ionization process retained for modelling atmospheric welding arc [45]. In an argon plasma with temperature ranging from 300 to $30000K$, the following impact ionization reactions can take place:

$$\begin{aligned} Ar \quad + x &\leftrightharpoons Ar^+ + e^- + x \\ Ar^+ + x &\leftrightharpoons Ar^{2+} + e^- + x \\ Ar^{2+} + x &\leftrightharpoons Ar^{3+} + e^- + x \end{aligned}$$

where x denotes the particle providing energy needed to promote ionization. The particle x is in most cases an electron accelerated by the electric field. The electrons entering the pre-sheath from the sheath indeed use to have energy significantly larger than the heavy particles. This ionization process is described by Saha equation. Different generalizations of the Saha equation do exist for two-temperature plasma or pre-sheath. A review was done by Rat et al. [45]. Some cathode layer models [30], [56] are based on the Saha generalization developed by Potapov [42] to calculate the plasma composition. Nowadays this formulation is no longer used since it was shown to be incorrect from a thermodynamic point of view [54] as well as from a kinetic point of view [13]. Zhou et al. [58], Coulombe and Meunier [16], and Cayla et al. [9, 8] use instead a formulation consistent with thermodynamic and kinetic law: the formulation proposed by Van de Sanden et al. [54] based on the electron temperature. Van de Sanden formulation is also used in this study to calculate the number density of five particles of argon plasma: $Ar, Ar^+, Ar^{2+}, Ar^{3+}, e^-$. To get these five unknown parameters, five equations are needed. The Dalton's law and electrical neutrality are also needed to close the system.

5.2.1 Saha equations based on the electron temperature

When the above impact ionization reactions are caused by an electron, the corresponding Saha equations generalized by Van de Sanden et al. [54] are

$$\begin{aligned}
\frac{n_e n_{Ar^+}}{n_{Ar}} &= 2\left(\frac{Q_{Ar^+}(T_e)}{Q_{Ar}(T_e)}\right)\left(\frac{2\pi\, m_e\, k\, T_e}{h_p^3}\right)^{\frac{3}{2}} \exp\left(-\frac{E_{i,Ar} - \Delta E}{k\, T_e}\right) \\
\frac{n_e n_{Ar^{2+}}}{n_{Ar^+}} &= 2\left(\frac{Q_{Ar^{2+}}(T_e)}{Q_{Ar^+}(T_e)}\right)\left(\frac{2\pi\, m_e\, k\, T_e}{h_p^3}\right)^{\frac{3}{2}} \exp\left(-\frac{E_{i,Ar^+} - \Delta E}{k\, T_e}\right) \\
\frac{n_e n_{Ar^{3+}}}{n_{Ar^{2+}}} &= 2\left(\frac{Q_{Ar^{3+}}(T_e)}{Q_{Ar^{2+}}(T_e)}\right)\left(\frac{2\pi\, m_e\, k\, T_e}{h_p^3}\right)^{\frac{3}{2}} \exp\left(-\frac{E_{i,Ar^{2+}} - \Delta E}{k\, T_e}\right)
\end{aligned} \tag{5.20}$$

where h_p is the Planck constant, m_e the electron mass, E_i the ionization energy of the considered argon particle, ΔE the lowering of the ionization energy and $Q(T_e)$ the internal partition function of the considered particle.

The lowering of the ionization energy (sometimes also called continuum lowering) results from the Coulomb field applied by ions and electrons on each ion present in the plasma [35]. It is given by Gleizes et al. [22]

$$\Delta E_{(l)} = (l+1)\frac{1}{4\pi\epsilon_0}\frac{e^2}{\lambda_D} \tag{5.21}$$

where l is the charge number, λ_D the Debye length and ϵ_0 the electric permittivity in vacuum. The internal partition function of an atom or atomic ion is defined as

$$Q = \sum_{j=1}^{P} g_j exp\left(-\frac{\epsilon_j}{kT}\right) \tag{5.22}$$

where P is the number of discrete energy levels, ϵ_j the energy of the discrete level j and g_j its degeneracy. The online toolbox of National Institute of Standard and Technology [34] is employed to retrieve the P, g_j and ϵ_j data for argon atom and ions. The resultant partition functions are plotted in Figure 5.4 for a pressure of one atmosphere.

5.2.2 Dalton's law

According to Boulos et al. [7] real gas effects can be neglected in thermal arc at atmospheric conditions. The pressure in the pre-sheath is then equal to the sum of the partial pressures of the individual gases, as stated by Dalton's law with partial pressures verifying the ideal gas law:

$$P = n_{Ar}kT_h + n_{Ar^+}kT_h + n_{Ar^{2+}}kT_h + n_{Ar^{3+}}kT_h + n_e kT_e \tag{5.23}$$

where $T_h = T_i$ is the temperature of heavy particles.

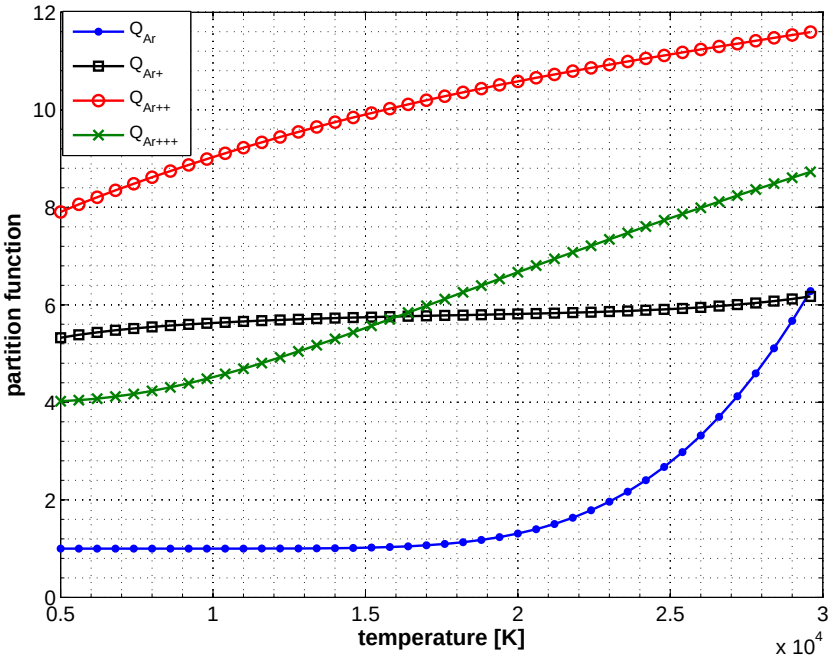

Figure 5.4: Argon partition functions at atmospheric pressure

5.2.3 Electric neutrality

As the pre-sheath satisfies local electro-neutrality, the electron density in the pre-sheath and at the sheath/pre-sheath interface is equal to the sum of all the ion densities weighted by their ion charge.

$$n_e = 1n_{Ar^+} + 2n_{Ar^{2+}} + 3n_{Ar^{3+}} \tag{5.24}$$

5.3 Temperatures and sheath voltage drop

To determine the electron temperature T_e at the sheath/pre-sheath interface, the cathode surface temperature T_c and the sheath voltage drop U_s a system of three equations needs to be solved. This system is built based on

1. the energy balance at the sheath/cathode interface,
2. the energy balance in the pre-sheath,
3. the current conservation at the cathode surface.

To be able to evaluate these equations some assumptions are made:

- The electron temperature in the sheath is almost equal to the one in the pre-sheath layer in the direction to the cathode surface [5]. Thus, one electron temperature is considered in the cathode layer.
- The LTE plasma is described through a one-temperature model [36].

5.3.1 Energy balance at the sheath/cathode interface

The total energy flux entering the cathode surface can be balanced with the heat flux transported towards the cathode bulk by thermal conduction [9]. The conduction flux in the cathode is

$$q^c_{cnd} = -\kappa_c \vec{\nabla} T. \tag{5.25}$$

The energy balance at the sheath/cathode interface is thus as follows:

$$q^c_{cath} = q^c_{cnd}. \tag{5.26}$$

To establish the energy balance equation at the cathode surface it is essential to identify the energy fluxes to and from the cathode surface. The energy fluxes at the sheath/cathode interface are illustrated in Figure (5.5). The energy brought to the cathode by neutrals coming from the plasma is neglected.

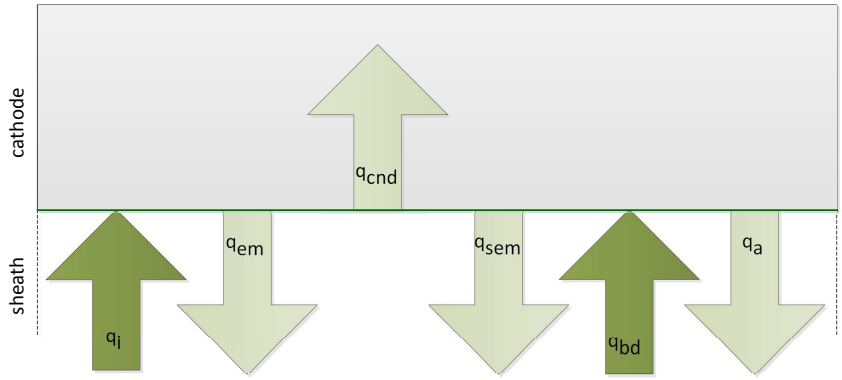

Figure 5.5: Fluxes at the cathode/sheath interface, q_i: ion flux, q_{em}: thermal-field emission flux, q_{cnd}: conduction flux, q_{sem}: secondary emission flux, q_{bd}: back diffusion flux and q_a: recombined ion flux

1. **Ion heating**
   The energy flux brought to the cathode surface by ions is defined based on the following assumptions:
   - The ions produced in the ionization layer have a velocity larger than the Bohm velocity when they enter the sheath [46].

- The ion current inside the sheath does not change with the distance to the cathode surface, since there is no ionization or recombination processes in this layer [50].
- The ions do not collide with any other particle in the sheath. The temperature of the ions in the sheath is thus equal to the temperature at the sheath/pre-sheath interface ($T_i = T_{is}$). The temperature of the heavy particles is continuous from the gas phase to the solid cathode [58], so $T_{is} = T_c$.
- All the kinetic energy of the ions is transferred to the cathode surface to be spent on electron emission.
- All the ions reaching the cathode surface do recombine.

The energy flux of ions towards the cathode q_i includes the kinetic energy brought to the cathode surface by the ions $(q_{KE})_i$, and the energy released to the surface by ion neutralization $(q_{ion})_i$. The kinetic energy flux of ions moving towards the cathode (so along y) is by definition

$$\begin{aligned}(q_{KE})_i = &\int_{v_x=-\infty}^{v_x=+\infty}\int_{v_y=-\infty}^{v_y=0}\int_{v_z=-\infty}^{v_z=+\infty} \\ &\frac{1}{2}m_i(v_x^2+v_y^2+v_z^2)v_y f_i(y,v_x,v_y,v_z)dv_x dv_y dv_z\end{aligned} \tag{5.27}$$

As partial LTE can be assumed in the pre-sheath, and according to the assumptions above listed, the velocity distribution of ions entering the sheath obey a Maxwellian distribution at the temperature $T_i = T_c$. Only ions with kinetic energy large enough can cross the space charge layer and reach the cathode surface. Therefore, the ion velocity distribution along the y-direction needs to be truncated to retain only ions with a large enough velocity u_y. Thus the motion of the ions in y-direction is not chaotic and the distribution in this direction cannot be Maxwellian. The ion distribution function $f_i(y, v_x, v_y, v_z)$ is equal to $f_i(y, v_y)f_M(v_x)f_M(v_z)$ where $f_i(y, v_y)$ is defined equation 5.10 and f_M denotes a standard Maxwellian distribution function. Then

$$f_i(y,v_x,v_y,v_z) = \begin{cases} \frac{n_{is}}{4\pi u_i^3}\exp\left(-\frac{v_x^2+v_z^2}{2u_i^2}\right) & if \quad -v_- > v_y > -v_+ \\ 0 & otherwise \end{cases} \tag{5.28}$$

where $u_i = \sqrt{kT_i/m_i}$ is the ion thermal velocity. The maximal and minimal velocity v_+ and v_- are

$$v_\pm = v_\pm(y) = \sqrt{(v_s \pm u_i)^2 - \frac{2Ze\varphi}{m_i}} \tag{5.29}$$

where v_s denoted Bohm velocity, and φ the electrostatic potential in the sheath. After integration, equations 5.27 and 5.28 lead to

$$(q_{KE})_i = n_{is} v_s (m_i u_i^2 + \frac{1}{2} m_i v_s^2 + \frac{1}{2} m_i u_i^2 + Ze\varphi) \tag{5.30}$$

The first term on the right hand side $n_{is}v_s$ is the ion current density J_i. The first term in bracket represents the average ion kinetic energy along the x- and z-direction, as expected for a Maxwellian distribution. The three last terms in bracket do represent the average ion kinetic energy along the y-direction. It differs very significantly from the kinetic energy $1/2kT_i$ a Maxwellian distribution would provide. The reasons are the following. The ion velocities along the y-direction are mono-directional, so restricted to $v_y \leq 0$. Their distribution is truncated to satisfy Bohm criteria. Finally the ion velocities are also accelerated by the electrostatic potential φ. The energy released to the surface by ion neutralization is

$$(q_{ion})_i = J_i (E_{ion} - Z\phi_{eff}) \tag{5.31}$$

where Z is the average ion charge ($Z = n_{es}/n_{is}$), ϕ_{eff} the effective work function, and E_{ion} the ionization/recombination energy of the ions recombined at the cathode surface.

$$E_{ion} = \frac{(E_{i,Ar^+})n_{Ar^+} + (E_{i,Ar^{2+}})n_{Ar^{2+}} + (E_{i,Ar^{3+}})n_{Ar^{3+}}}{n_{Ar^+} + n_{Ar^{2+}} + n_{Ar^{3+}}} \tag{5.32}$$

It means that the cathode gains some energy when ions recombine (first term in the bracket). The ions recombine with electrons extracted form the cathode. Electron extraction consumes energy equal to the work function of the cathode (second term in the bracket). On the cathode surface the electrostatic potential is the sheath potential drop $\varphi = U_s$. The total ion energy flux to the cathode $q_i = (q_{KE})_i + (q_{ion})_i$, is thus

$$q_i^c = J_i \left(\overbrace{\underbrace{2kT_{is}}_{I} + \underbrace{\frac{kZT_e}{2}}_{II} + \underbrace{ZeU_s}_{III}}^{kinetic\ energy} + \overbrace{\underbrace{E_{ion}}_{IV} - \underbrace{Z\phi_{eff}}_{V}}^{ion\ neutralization} \right). \tag{5.33}$$

In the text book Plasma Physics and engineering [21] the last three terms (III, IV, V) are mentioned. The same equation as (5.33) is employed for ion heating by Benilov [5] and Wendelstorf [56]. Cayla et al. [9] do not use the term (I) which is apparently cancelled by back flow recombined ions (see equation (5.37)). Zhou and Heberlein [58] add up the terms (I, II) since they develop a one-temperature model. Tashiro et al.[52] employed only the term (IV) in their calculation.

2. **Electron emission cooling**
   The electrons emitted, either by thermal-field emission or by secondary emission, transfer their energy from the cathode surface to the sheath, according to

$$q_{em}^{c} = -J_{em}\left(\phi_{eff} + 2kT_c\right), \tag{5.34}$$

$$q_{sem}^{c} = -J_{sem}\left(\phi_{eff} + 2kT_c\right), \tag{5.35}$$

   where J_{em} is the thermal-field emission current density of equation (5.2) and J_{sem} is the secondary emission current density of equation (5.16). The first contribution to the energy transferred from the cathode by electrons is the effective work function. The second contribution is the kinetic energy of electrons. It is obtained assuming that the electrons are heated with the cathode surface ($T_e = T_c$) and their distribution function is a Maxwellian reduced to half the velocity space concerning the y-direction.

   Cayla et al.[9] used the same expresion for q_{em} and q_{sem}. Benilov [5] did not take into account the secondary emission. In the work by Wendelstorf [56] and Tashiro et al. [52], the secondary emission and the thermal energy of the electrons are both ignored. Zhou and Heberlein [58] neglected the secondary emission and used $2.5kT_c$ for the thermal energy.

3. **Back diffusion electron heating**
   The electrons coming from the ionization layer with enough energy ($v_y \leq -\sqrt{\frac{2eU_s}{m_e}}$) can pass the sheath voltage drop, and reach the cathode surface. This produces a flux of energy to the cathode

$$q_{bd}^{c} = J_{bd}\left(\phi_{eff} + 2kT_e\right). \tag{5.36}$$

   The last term or flux of kinetic energy, involves again a factor 2 since the electron velocities along the y-direction are restricted to $v_y \leq 0$.

   The same equation is employed in most of the reports [5, 56, 9]. However, Zhou and Heberlein [58] used $2.5kT_e$ for the kinetic energy part.

4. **Recombined ions cooling**
   The ions reaching the cathode surface recombine and may go back towards the plasma. This forms a cooling heat flux by recombined atoms, q_a^c. Based on the assumption that all of the ions are neutralized at the cathode surface, this cooling heat flux is equal to

$$q_{a}^{c} = -J_i\left(2kT_c\right). \tag{5.37}$$

Benilov [5] and Wendelstorf [56] used the same equation. Cayla et al. [9] do not mention the energy flux of recombined ions, but they do not either consider the term (I) of ion flux in equation (5.33).

5. **Thermal radiation cooling**
   Lichtenberg et al. [37] showed that for cathode surface temperature less than $2500K$ the radiation is negligible and Lago et al. [36] indicated that for cathode surface temperature more than $2500K$ the radiation from the cathode surface is cancelled by the radiation from the bulk plasma to the cathode surface. Therefore, the radiation is not considered in this study. Thermal radiation is neglected in the works by Benilov [5], Zhou et al. [58], and Cayla et al. [9].

Now the total energy flux to the cathode surface due to ion heating, emission cooling, electron back diffusion heating and recombined ion back flow cooling can be estimated according to

$$\begin{aligned} q^c_{cath} = &+ J_i(\frac{kZT_e}{2} + ZeU_s + E_{ion} - Z\phi_{eff}) \\ &- (J_{em} + J_{sem})\,(\phi_{eff} + 2kT_c) \\ &+ J_{bd}\,(\phi_{eff} + 2kT_e) \end{aligned} \tag{5.38}$$

5.3.2 Energy balance in the pre-sheath

To establish the energy balance equation in the ionization layer the energy fluxes at its boundaries need to be identified. All the possible heat fluxes are showed in Figure (5.6). It can be seen that the energy balance in the pre-sheath can be described as follows:

$$q^{ps}_{em} + q^{ps}_{sem} + W^{ps}_E = q^{ps}_{bd} + q^{ps}_i + q^{ps}_e \tag{5.39}$$

1. **Ionization cooling**
   Ionization cooling includes two components. The first is within the pre-sheath and corresponds to ionization energy sink. As all the ions produced by impact ionization in the pre-sheath move towards the cathode with the current density J_i, the ionization energy sink is $J_i E_{ion}$ with E_{ion} defined equation (5.32). The second component is the energy transported away by the ions as they move towards the sheath. It is the energy term $(q_{KE})_i$ of equation (5.30) at the sheath/pre-sheath interface with $\varphi = 0$ because of local electro-neutrality so that $(q_{KE})_i = J_i(2kT_i + \frac{kZT_e}{2})$. As a result the total cooling in the pre-sheath because of ionization is

$$q^{ps}_i = -J_i\left(2kT_i + \frac{kZT_e}{2} + E_{ion}\right) \tag{5.40}$$

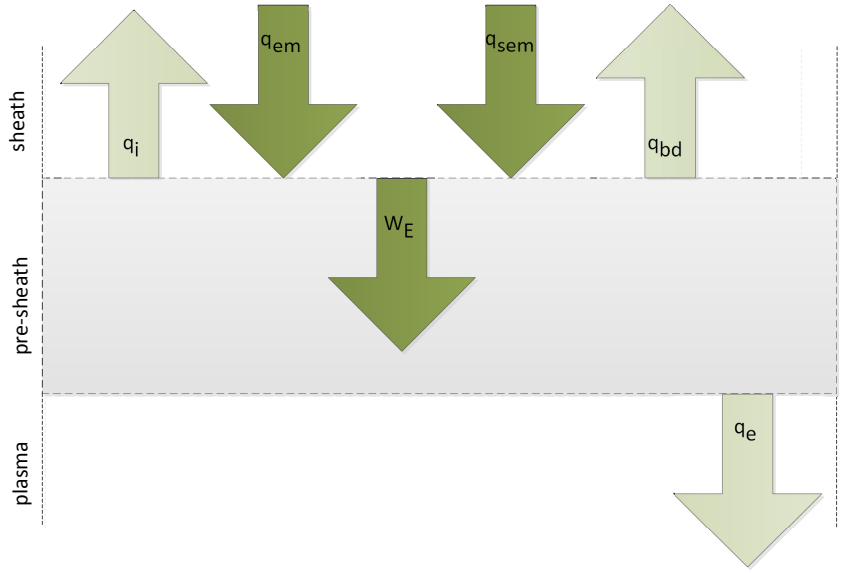

Figure 5.6: Fluxes in the ionization layer, q_i: ion flux, q_{em}: thermal-field emission flux, W_E: work of electric field, q_{sem}: secondary emission flux, q_{bd}: back diffusion flux and q_e: electron flux to the plasma

Equation (5.40) is thus built to satisfy energy conservation at the sheath/pre-sheath interface. In the work done by Benilov [5], Wendelstorf [56] and Cayla et al. [9] the first two terms which represent the kinetic energy are not considered. Zhou and Heberlein [58] used $2.5kT_c$ since they consider a one-temperature model $T_e = T_c$.

2. **Emitted electrons heating**
   The emitted electrons accelerated in the sheath by the sheath voltage drop U_s transport their energy to the ionization layer. Considering thermal-field and secondary emission current density (equations (5.2), (5.16)), the heat flux to the ionization layer can de described with the two equations

$$q_{em}^{ps} = +J_{em}\left(2kT_c + eU_s\right) \tag{5.41}$$

$$q_{sem}^{ps} = +J_{sem}\left(2kT_c + eU_s\right) \tag{5.42}$$

   The first term in bracket is the thermal energy of the electrons moving from the cathode. The second term refers to the work done on the electrons by the sheath voltage drop U_s. The secondary emission J_{sem} is only considered by Cayla et al. [9].

3. **Back diffusion electron cooling**
   Electrons having enough energy can leave the ionization layer, pass the

potential barrier of the sheath layer and reach the cathode. The flux of energy carried away by these electrons is described by

$$q_{bd}^{ps} = -J_{bd}\,(2kT_e + eU_s) \tag{5.43}$$

The first term in the bracket is the thermal energy of the electrons (see explanations in part 2 section 5.3.1) and the second term refers to the fact that the electrons with the kinetic energy eU_s are able to go through the sheath potential barrier towards the cathode.

4. **Electrons cooling**
   According to Benilov and Marotta [5] the flux of the energy carried away by the electrons leaving the ionization layer to the bulk plasma is equal to

$$q_e^{ps} = -3.2 J_{tot} k T_e \tag{5.44}$$

where J_{tot} represents the total current density, equation (5.1). The coefficient 3.2 includes two contributions. A factor 2.5 accounting for enthalpy transport resulting from the electric current. The rest is a thermal-diffusion coefficient calculated for a strongly ionized plasma [5].

5. **The work of the electric field**
   Emitted electrons enter the pre-sheath (from the sheath) with the current density $J_{em} + J_{sem} - J_{bd}$ and move away from the pre-sheath towards the plasma with the current density J_{tot}. The average current density across the pre-sheath is thus $\frac{1}{2}(J_{em} + J_{sem} - J_{bd} + J_{tot})$. These electrons move in an electric field produced by the ionization layer voltage drop U_i. They thus produce an average work defined by

$$W_E^{ps} = +\frac{(J_{sem+}J_{em} - J_{bd}) + J_{tot}}{2} U_i \tag{5.45}$$

where J_{tot} is the total current density, equation (5.1). The voltage drop in the ionization layer can be described as follows [5]:

$$U_i = \frac{kT_e}{e} \ln \frac{n_{e\infty}}{n_{es}}, \tag{5.46}$$

where $n_{e\infty}$ represents the number of electron density at the plasma edge and n_{es} is the number of electron density at the sheath edge. The expression 5.46 was obtained by Benilov and Marotta [5] using an estimation of the ion number density at the sheath/pre-sheath interface. This estimation can be used when the ionization degree of the ionization layer is between about 0.6 to 1. Referring to the Figure 2.2, it means that $T_e \geq 15000K$. According to Benilov and Marotta [5], at lower ionization degree the pre-sheath cannot remain in static equilibrium. However, this non-equilibrium effect is not taken into account when $\alpha < 0.6$, and equation (5.46) is used for any ionization degree.

Combining the results, the energy balance in the ionization layer reads

$$\begin{aligned}
&(J_{em} + J_{sem}) \left[2kT_c + eU_s + kT_e \left(\ln \frac{n_{e\infty}}{n_{es}} - 3.2 \right) \right] \\
&= J_{bd} \left[eU_s + kT_e \left(\ln \frac{n_{e\infty}}{n_{es}} - 1.2 \right) \right] \\
&+ J_i \left[2kT_i + E_{ion} + ZkT_e \left(3.7 - 0.5 \ln \frac{n_{e\infty}}{n_{es}} \right) \right].
\end{aligned} \tag{5.47}$$

Equation (5.47) is based on Benilov's study [5] supplemented by the work of Cayla et al. [8] with the additional contribution of secondary emission, J_{sem}. The difference between equation (5.47) and the study by Cayla et al. comes from the ionization sink energy (5.40) which has additional terms regarding the kinetic energy. It changes the last term in equation (5.47) which has an additional factor of $2kT_i$ and coefficient of 3.7 instead of 3.2. These additional terms allows satisfying energy conservation at the sheath/pre-sheath interface.

5.3.3 Current conservation

The conservation of the current density at the cathode surface writes

$$J_{cath} = e(ZJ_i + J_{em} + J_{sem} - J_{bd}). \tag{5.48}$$

J_{cath} is the total current at the cathode surface. It is made up of the contribution of the positive ion current density J_i, the negative back diffusion current density J_{bd} going into the cathode surface, as well as the negative emission current densities J_{em} and J_{sem} leaving the cathode surface. Comparing equation (5.48) with (5.1) we can see that $J_{cath} = J_{tot}$. The total current at the cathode surface J_{cath} is the input parameter in our model (see Figure 5.7). Assuming an homogeneous distribution of the current density in the electrode of cross sectional area A_{cath}, and a total electric current intensity I, J_{cath} is

$$J_{cath} = \frac{I}{A_{cath}}. \tag{5.49}$$

5.4 Calculation procedure

The flowchart of the calculation algorithm is showed in Figure (5.7). The aim of the model is to calculate the total heat flux from the cathode layer to the cathode surface, q_{cath}. The input value is the current density at the cathode J_{cath}. For a given electric current I and cross sectional area of the cathode A_{cath}, the cathode current density J_{cath} is calculated from equation (5.49). Initial guesses of

the electron temperature T_{e0} at the sheath/pre-sheath interface, the cathode surface temperature T_{c0}, and the sheath voltage drop U_s are used in the set of Saha equations (5.20), Dalton's law (5.23) and the electric neutrality equation (5.24) to calculate the number density of electron n_{es} and Ar^+ ions n_{Ar^+}. It should be noted that the number density of electrons in the plasma core ($n_{e\infty}$) is calculated with the same set of equations setting $T_e = T_c$ since the plasma core is in LTE. The equations (5.2-5.19) are then employed to calculate the current densities of the particles $J_i, J_{em}, J_{sem}, J_{bd}$. Finally by resolving the set of non-linear equations for energy and current density conservation (5.26), (5.47), (5.48) with the given J_{cath}, new values for the electron temperature, cathode temperature and sheath voltage drop are obtained. These new values are compared with the previous values, and iteration is continued until convergence.

5.5 Numerical procedure

To follow the calculation procedure mentioned in the previous section, two sets of non-linear equations should be solved (see Figure 5.7). In this study both systems of non-linear equations are solved using the Newton-Raphson algorithm, namely $x_{n+1} = x_n - J^{-1}.f(x_n)$. There x denotes the root of the function f and J is the numerical Jacobian matrix. However, due to numerical problems caused by high non-linearity and manipulation of very large numbers (greater than the order of 10^{20}) the convergence of the algorithm is not easy to achieve.

Both sets of equations deal with very small or very large quantities and numbers. For instance, the Planck constant (of the order of 10^{-34}), the Boltzman constant (of the order of 10^{-23}), the electron mass (of the order of 10^{-31}) and the number densities (of the order of 10^{+24}). This can cause problems to approach the convergence criterion of the solution, and can also produce some inaccuracy by reaching precision of the computer or the solver. To avoid such problems, the molar concentrations are used instead of number densities. The molar concentration is the number density divided by Avogadro number, N_A.

For resolving the first system of non-linear equations (set-1 in Figure 5.7) the methodology used by Godin [23] is employed. This method is based on the concept of the chemical basis. A chemical basis is a subset of species from which all other species may be formed by means of chemical reaction [23]. In our model the species constituting the basis would be argon atoms and electrons of densities n_{Ar} and n_e, respectively. The ionization reactions (by impact ionization) write

$$
\begin{aligned}
Ar + e^- &\leftrightharpoons Ar^+ + 2e^- \\
Ar^+ + e^- &\leftrightharpoons Ar^{2+} + 2e^- \\
Ar^{2+} + e^- &\leftrightharpoons Ar^{3+} + 2e^-.
\end{aligned}
$$

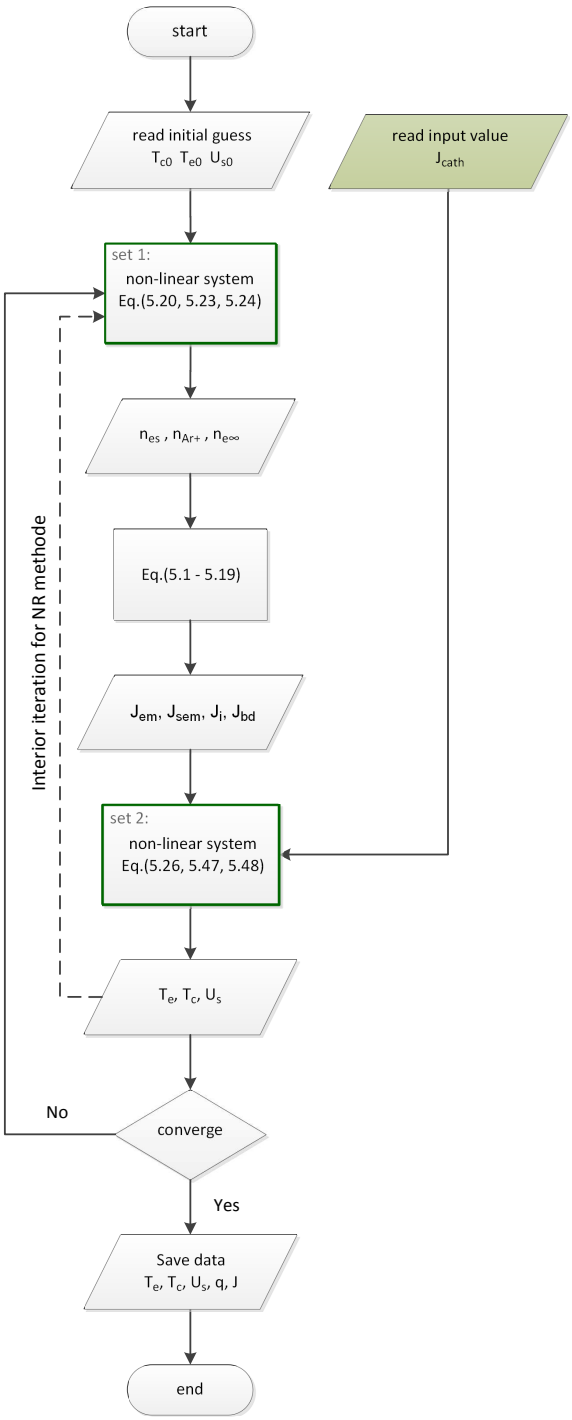

Figure 5.7: The calculation algorithm flowchart

Thus, the set of Saha equations based on the basic species can be rewritten as

$$
\begin{aligned}
n_{Ar^+} &= \left(\frac{n_{Ar}}{n_e}\right)(K1) \\
n_{Ar^{2+}} &= \left(\frac{n_{Ar}}{n_e^2}\right)(K1)(K2) \\
n_{Ar^{3+}} &= \left(\frac{n_{Ar}}{n_e^3}\right)(K1)(K2)(K3)
\end{aligned}
\tag{5.50}
$$

where $K1, K2$ and $K3$ are the right hand side of the corresponding Saha equations (5.20). Now by replacing $n_{Ar^+}, n_{Ar^{2+}}, n_{Ar^{3+}}$ in equations (5.20), (5.23), (5.24) with their equivalent from equation (5.50) we end up with two equations and two variables (n_e, n_{Ar}) which can be resolved using the Newton-Raphson method. The calculated plasma compositions is illustrated in Figure 6.1 for an LTE plasma ($T_i = T_e$).

The second set of non-linear equations (set-2 in Figure (5.7)) includes two energy balance equations in addition of a current conservation equation. For the second set, the methodology by Godin does not apply. The system is highly non-linear and produces a complex Jacobian matrix which is problematic regarding the numerical iteration. Therefore, the system of non-linear equation is solved with the Secant method which is basically the Newton-Raphson algorithm, but approximating the Jacobian matrix through finite differences.

Chapter 6

Cathode layer - results

In this section a parametric study of the most important parameters of the cathode region is done. These parameters are the current density, the heat fluxes to the cathode, the cathode voltage drop, and the cathode surface temperature. Since the cathode layer model is developed based on the work by Cayla et al [9], the results obtained here are compared with the results of Cayla. As mentioned in section (5.3.2), Cayla et al [9] do not consider some kinetic energy terms (of the ionization heat flux) in the energy balance of the ionization layer. Thus the last term in the right hand side of equation (5.47) changes to

$$+J_i \left[E_{ion} + ZkT_e \left(3.2 - 0.5 \ln \frac{n_{e\infty}}{n_{es}} \right) \right],$$

in Cayla's model.

The calculations are performed using an argon gas at atmospheric pressure with a $1cm$ high tungsten cathode. The following assumption have been made:

- The cathode is water cooled to $1000K$.
- The cathode does not evaporate. This assumption seems reasonable as tungsten has a boiling temperature larger than $5933K$ and a melting of $3683K$.

To be able to compare the results with those of Cayla, a range of $1 \times 10^4 - 5 \times 10^8 A.m^2$ is chosen for the cathode current density (the input parameter). The calculation model was implemented in MATLAB 7.11.0.

The first step in our modelling procedure (see Figure 5.7) is the calculation of the plasma composition. Figure 6.1 shows the plasma composition against the temperature for a LTE plasma ($T_e = T_i$), so at the plasma/pre-sheath interface. Figure 6.2 (resp. 6.3) shows a comparison of the argon atom (resp. electron)

density at two different locations: the LTE plasma/pre-sheath interface and the non-LTE pre-sheath/sheath interface. These figures clearly show the decrease in number of neutral atoms and the increase in number of electrons when the cathode current density increases. They also show the difference in plasma composition at the LTE plasma/pre-sheath interface and at the non-LTE pre-sheath/sheath interface, as expected for an ionization layer.

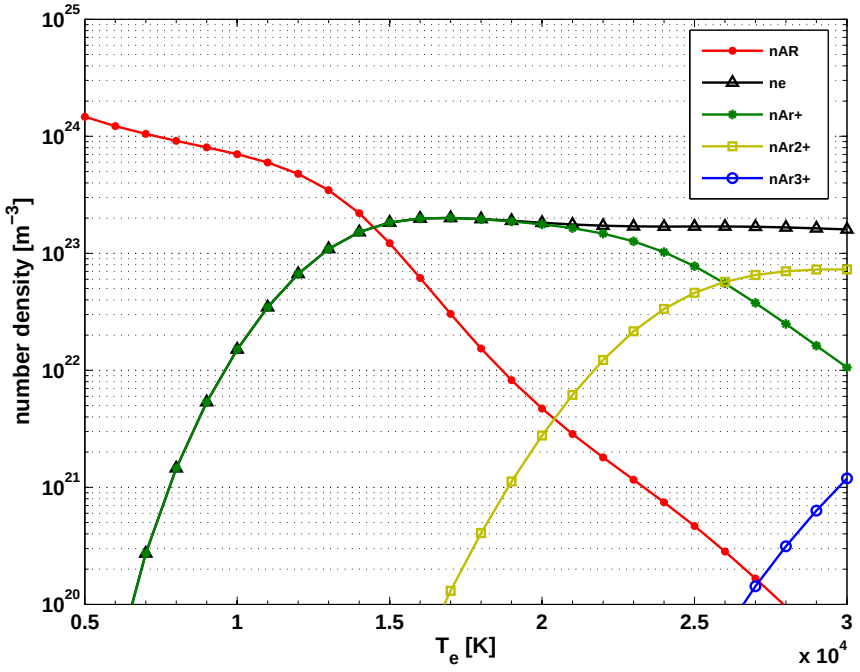

Figure 6.1: plasma composition in LTE at atmospheric pressure

Figure 6.4 illustrates the current densities in the sheath plotted versus the cathode current density J_{cath}. It can be seen that the ion current density J_i increases almost linearly with J_{cath}. It is also the dominant current density in the cathode layer. Figure 6.5 shows the cathode temperature T_C. Figure 6.7 and 6.6 show the voltage drop U_s in the sheath and U_i in the pre-sheath. It can be seen on these figures that the potential voltages U_s and U_i are largest at low current density, when the temperature T_c of the cathode surface is low. In these conditions the cathode surface is too cold to promote any significant thermoionic emission: J_{em} is also low. The dominant emission process is then secondary emission. The secondary emission current density J_{sem} has indeed a larger value compared to the thermal field emission J_{em} when the cathode current density is less than $3 \times 10^5 A.m^{-2}$. The back diffusion current density J_{bd} is almost negligible for cathode current density smaller than $5 \times 10^6 A.m^{-2}$.

The cathode surface temperature increases significantly for the range of cur-

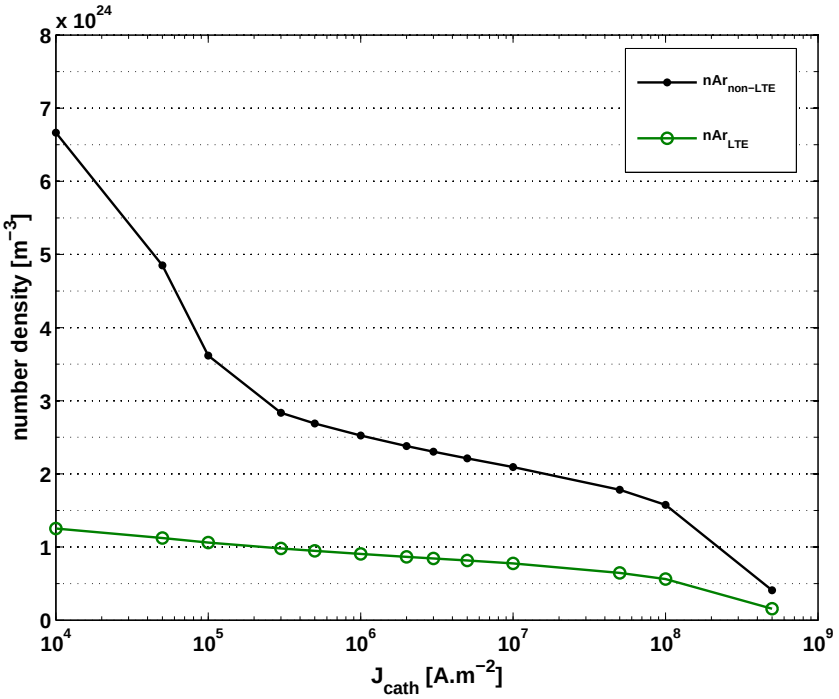

Figure 6.2: Argon number density in LTE and non-LTE at atmospheric pressure

rent density $10^4 - 10^6 A.m^{-2}$. Similarly, the emission current density increases significantly from zero to $10^5 A.m^{-2}$ for this same range of current density J_{cath}. These temperature and thermal-field emission current changes are associated with dramatic changes in the sheath voltage drop U_s and the pre-sheath voltage drop U_i. These changes correspond to the transition area between glow regime ($10^5 A.m^{-2}$) and the thermionic regime.

The thermionic regime is established for current densities where the sheath voltage drop remains almost constant [58]. It can be seen in Figure 6.7 that the thermionic regime is established for current densities above $10^7 A.m^{-2}$ from which U_s stays at a value of $10V$.

Figure 6.8 shows the total heat flux to the cathode and its components. It can be seen that the ion heat flux is always the leading heating process. It can also be seen that up to $10^6 A.m^{-2}$ of current density, the total heat flux to the cathode is almost equal to the ion heat flux to the cathode. It can be observed that the contribution of the secondary emission heat flux q_{sem} to the total heat flux is significant for a cathode current density less than $5 \times 10^5 A.m^{-2}$, thus a cathode surface temperature of $2700K$ or less. For a cathode current density higher than $2 \times 10^5 A.m^{-2}$ one can see that despite increasing the current density, the total heat flux remains constant at about $2 \times 10^7 W.m^{-2}$. This constant heat flux to the cathode, see Figure 6.5, causes a linear increase in cathode temperature for the

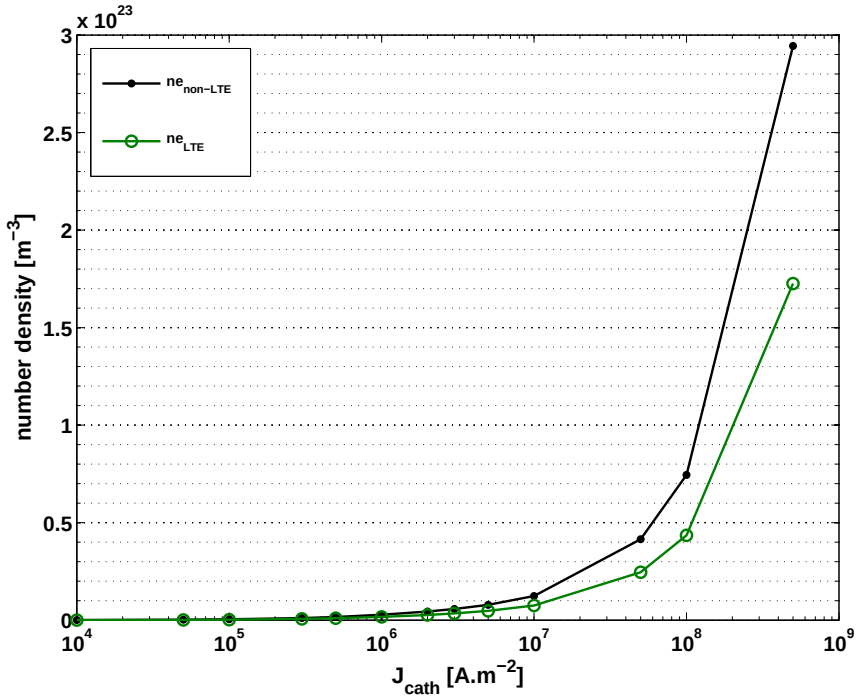

Figure 6.3: Electron number density in LTE and non-LTE at atmospheric pressure

cathode current density higher than $2 \times 10^5 A.m^{-2}$. It is worth reminding that melting is not considered in this study which makes it possible in our model for the cathode surface to reach $5300K$ while the tungsten melting point is $3682K$.

Figure 6.9 shows that as the cathode current density increases the electron temperature rises and can reach up to maximum $14400K$ for a $5 \times 10^8 A.m^{-2}$ cathode current density.

The results of the present study are compared to the work by Cayla et al [9]. The electron temperature against the cathode current density is plotted in Figure 6.10. It can be seen that there is a small difference (almost $400K$) between the results of this study and the results of Cayla. To be able to see the effect of terms added in the energy balance equation (5.47), the calculations are also done negelecting these terms and plotted with the legend "Cayla equations". Figure 6.10 shows that the added terms have almost no effect on the electron temperature. Figures 6.12 and 6.11 which represent the cathode temperature and the sheath voltage drop respectively show a good agreement with Cayla's study.

To conclude, the main characteristics calculated with the interface layer model are in good agreement with the reference literature. The electron temperature,

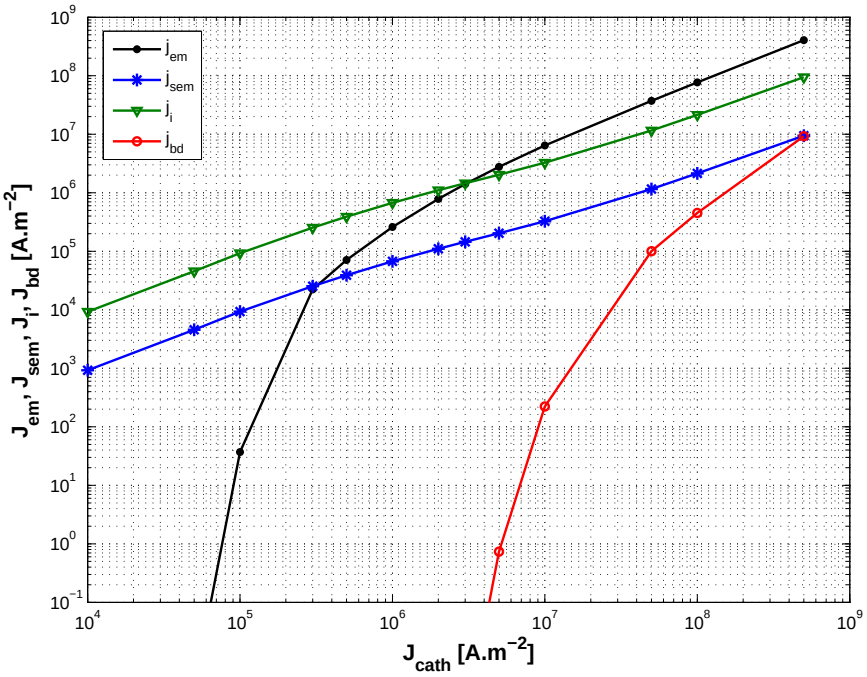

Figure 6.4: Current density components against cathode current density.

however, has a small deviation from the reference study. It has been showed that the changes in the energy balance equation done in this study do not have effect on this deviation. This small deviation could be due to the different data used for calculating the partition functions used in the model (see section 5.2.1).

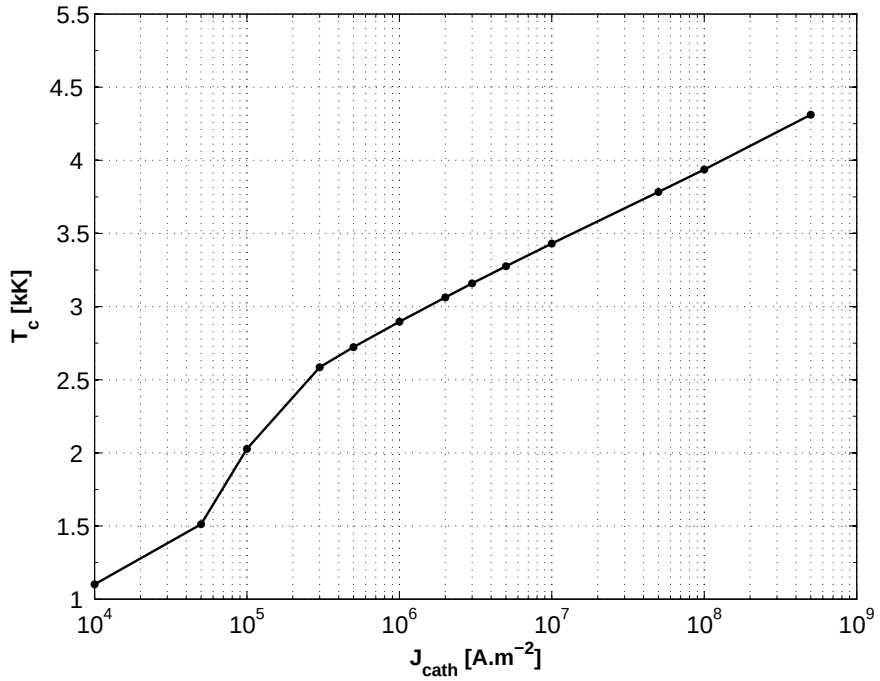

Figure 6.5: Cathode temperature against cathode current density.

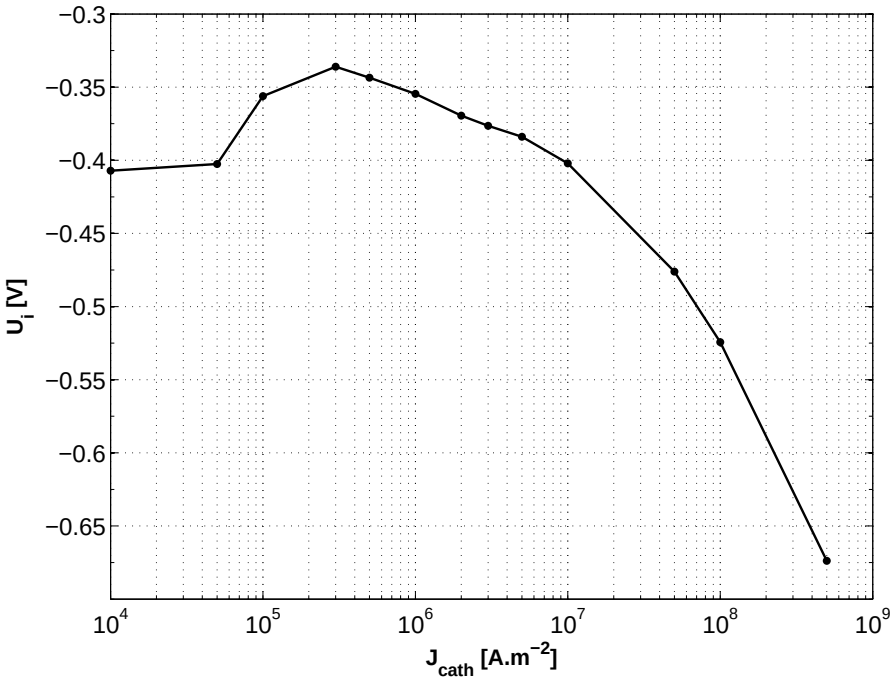

Figure 6.6: Pre-sheath voltage drop against cathode current density.

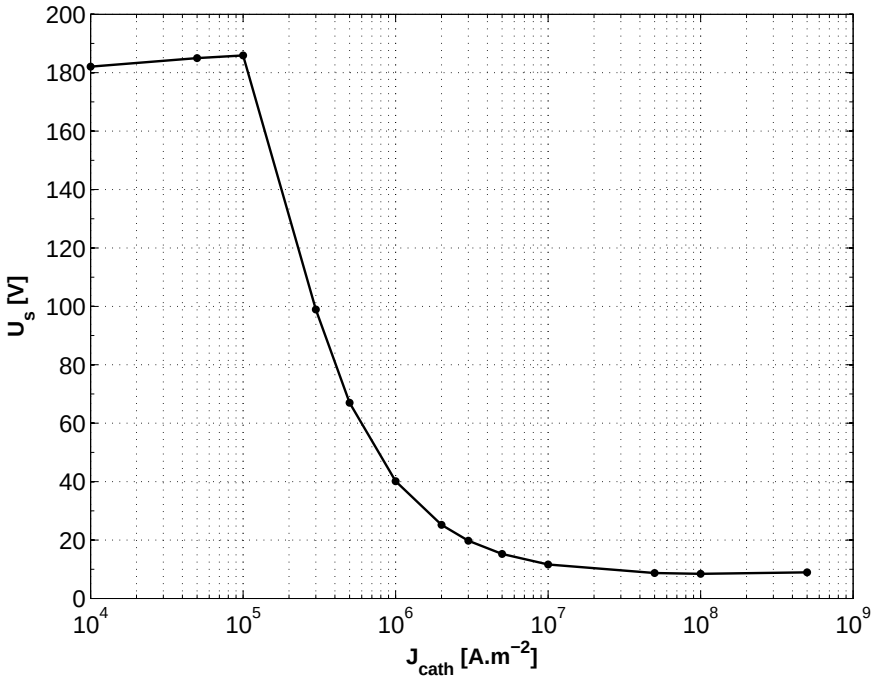

Figure 6.7: Sheath voltage drop against cathode current density.

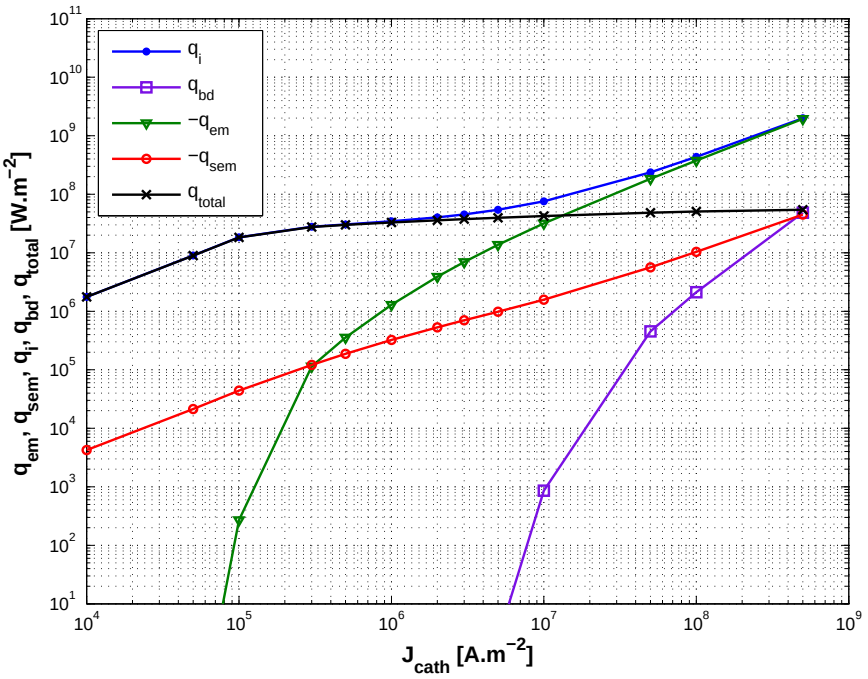

Figure 6.8: Heat flux against cathode current density.

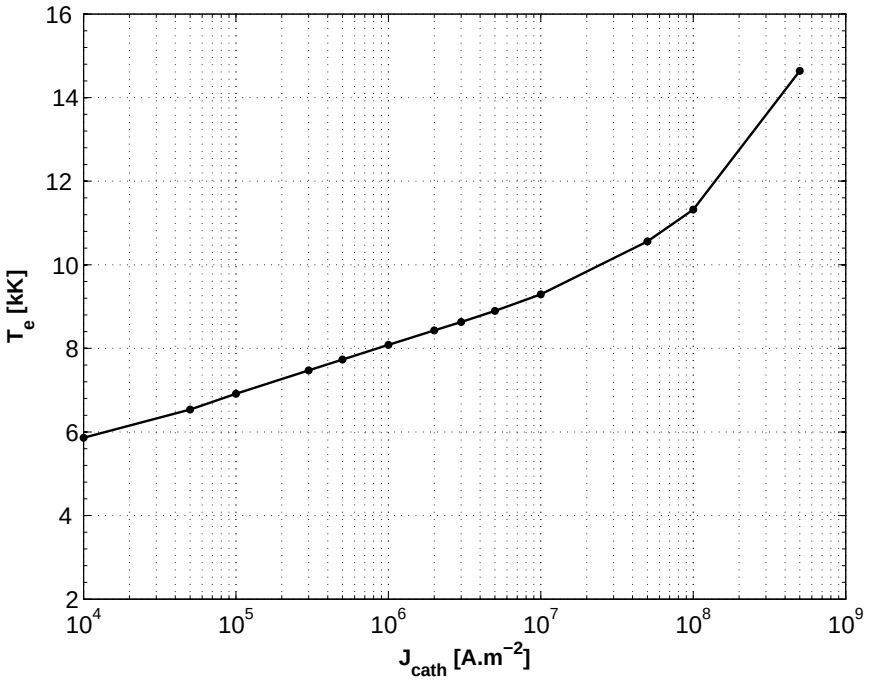

Figure 6.9: Electron temperature against cathode current density.

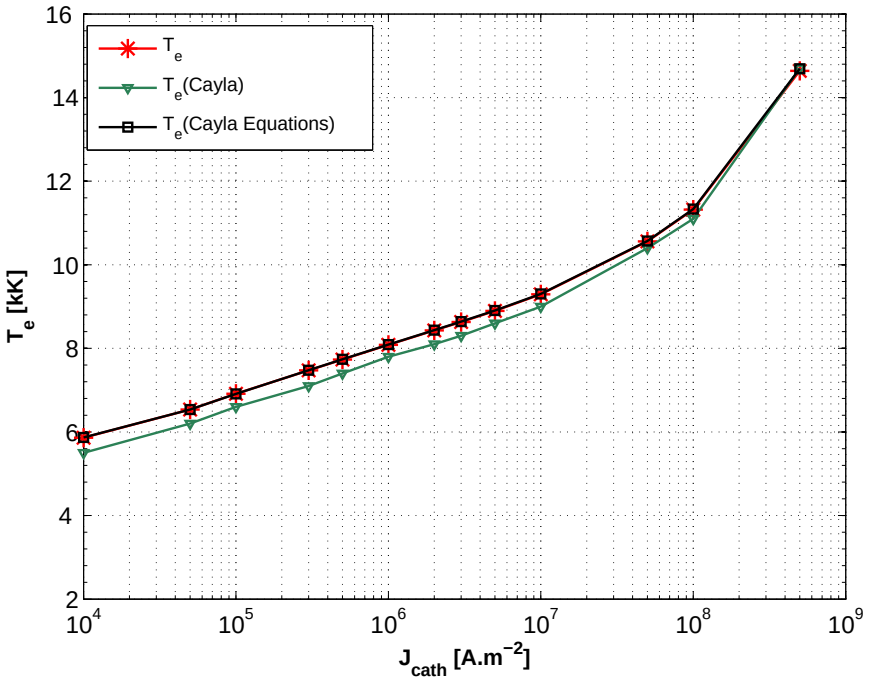

Figure 6.10: Electron temperature against cathode current density.

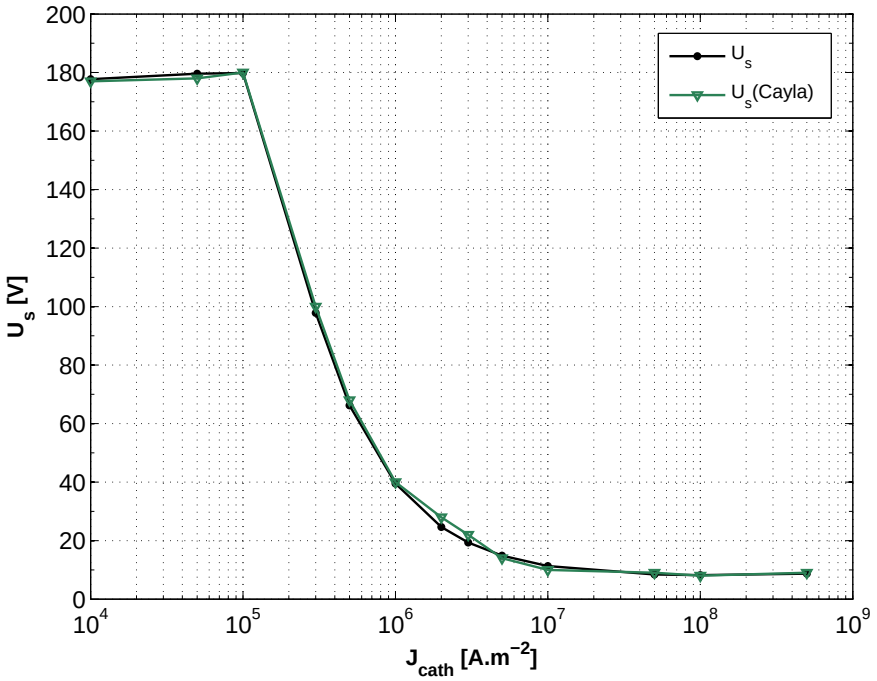

Figure 6.11: Sheath voltage drop against cathode current density.

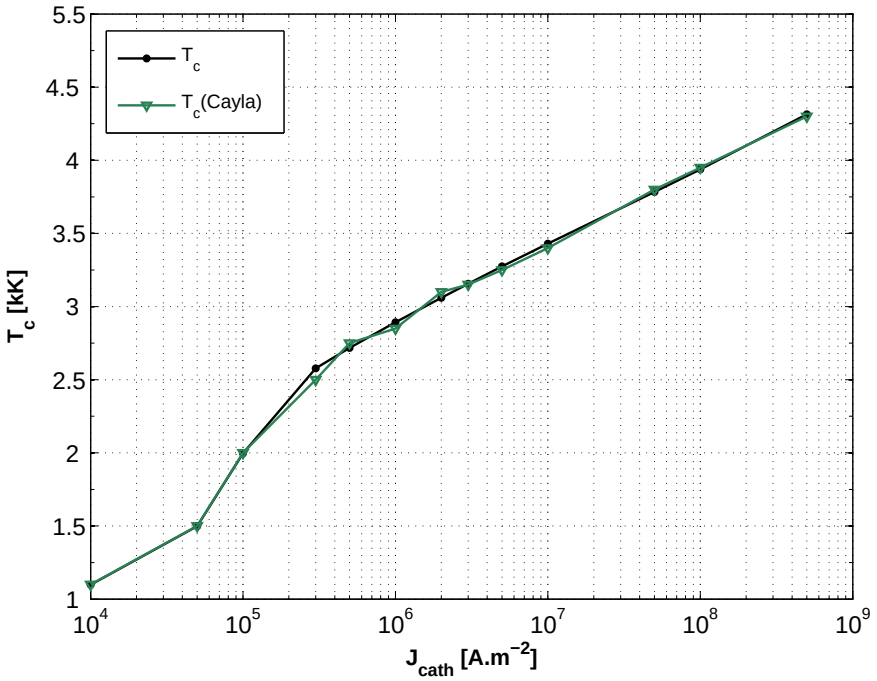

Figure 6.12: Cathode temperature against cathode current density.

Chapter 7

Conclusion and perspective

The aim of the present work was to go one step further in the development of a predictive arc simulation model. A predictive tool would indeed allow improving the understanding of the welding arc process, and thereby increase the opportunities to better control it. It would also allow providing the heat input data needed for investigating numerically the behaviour of the weld pool, changes in the materials microstructure and properties during welding, and residual stress and temperature evolution of welds. To be predictive, the arc model should be free of boundary conditions on the anode and cathode surfaces, as these conditions are difficult to measure and inaccurate while they they do have a very significant influence on the arc. To overcome this constraint, the arc needs to be supplemented with the anode and cathode into the simulation model.

To go one step further towards the coupled model, the concepts of plasma and arc discharges useful for this problem has been reviewed. The main sub-regions of the model and their dominant physical roles has been discussed.

The coupled arc-electrode model has been developed in different steps. First coupling solid and fluid regions for a simpler problem without complex coupling interface. This has been applied to a laser welding problem using the solver chtMultiRegionFoam of the CFD software OpenFOAM. The flow of the laser welding shielding gas over the base metal with both shielding pipe and shielding plate has been studied. The results confirmed that the shielding plate provides a good protection of the cooling weld against the surrounding atmosphere. The shielding screen produced by the plate has a negligible influence on the cooling rate of the weld. However, the design of the shielding pipe and plate is in conflict with the requirements of the optical system for tracking the welding path. It has been concluded that the design of the pipe and plate should be modified to deflect differently the shielding gas flow.

The extension of the OpenFOAM solver chtMultiRegionFoam to a welding arc model coupling the plasma arc heat source with the electrode and base metal has then been undertaken implementing a coupled electromagnetic model for

the solid and fluid region. This technical part was not detailed here and can be found in the report [32].

Then, the modelling of the cathode layer has been addressed. Different modelling approaches available in the literature have been studied to determine their advantages and drawbacks. One of them developed by Cayla has been used and further improved so as to satisfy the basic principles of charge and energy conservation in the different regions of the cathode layer. A numerical procedure has been presented and implemented in MATLAB. It has been tested for different arc core and cathode conditions. The main characteristics calculated with the interface layer model are in good agreement with the reference literature. The electron temperature, however, has a small deviation from the reference study. It has been shown that the changes in the energy balance equation done in this study do not have effect on this deviation. This small deviation could be due to the different data used for calculating the partition functions used in the model (see section 5.2.1).

The future development will be the implementation of the interface layer model in OpenFOAM, and its validation by comparison with experimental data. Next, the calculations will be done for tilted electrode. The tilt angle is an important parameter influencing the temperature distribution. However, there is no experimental measurement available for setting the boundary conditions on the cathode (and anode) surface for tilted electrode. An arc produced by a tilted electrode is thus a typical application requiring a coupled arc-cathode model to be calculated.

References

[1] M.S. Benilov. Theory and modelling of arc cathodes. *Plasma Sources Science and Technology*, 11(3A):A49, 2002.

[2] M.S. Benilov. Understanding and modelling plasma–electrode interaction in high-pressure arc discharges: a review. *Journal of Physics D: Applied Physics*, 41(14):144001, 2008.

[3] M.S. Benilov, M. Carpaij, and M.D. Cunha. 3D modelling of heating of thermionic cathodes by high-pressure arc plasmas. *Journal of Physics D: Applied Physics*, 39(10):2124, 2006.

[4] M.S. Benilov, M.D. Cunha, and G.V. Naidis. Modelling interaction of multispecies plasmas with thermionic cathodes. *Plasma Sources Science and Technology*, 14(3):517, 2005.

[5] M.S. Benilov and A. Marotta. A model of the cathode region of atmospheric pressure arcs. *Journal of Physics D: Applied Physics*, 28(9):1869, 1995.

[6] R. Bini, M. Monno, and M.I. Boulos. Numerical and experimental study of transferred arcs in argon. *Journal of Physics D: Applied Physics*, 39(15):3253, 2006.

[7] M.I. Boulos, P. Fauchais, and E. Pfender. *Thermal plasmas*, volume 1. Plenum Publishing Corporation, 1994.

[8] F. Cayla. *Modélisation de l'interaction entre un arc électrique et une cathode*. PhD thesis, Université de Toulouse, Université Toulouse III-Paul Sabatier, 2008.

[9] F. Cayla, P. Freton, and J.J. Gonzalez. Arc/cathode interaction model. *Plasma Science, IEEE Transactions on*, 36(4):1944–1954, 2008.

[10] I. Choquet, P. Degond, B. Lucquin-Desreux, et al. A hierarchy of diffusion models for partially ionized plasmas. 2007.

[11] I. Choquet, A. Javidi, and H. Nilsson. On the choice of electromagnetic model for short high-intensity arcs, applied to welding. *Journal of Physics D: Applied Physics*, 45(20):205203, 2012.

[12] I. Choquet and B. Lucquin-Desreux. Hydrodynamic limit for an arc discharge at atmospheric pressure. *Journal of statistical physics*, 119(1):197–239, 2005.

[13] I. Choquet and B. Lucquin-Desreux. Non equilibrium ionization in magnetized two-temperature thermal plasma. 2010.

[14] I. Choquet and B. Lucquin-Desreux. Non equilibrium ionization in magnetized two-temperature thermal plasma. *Kinetic and Related Models*, 4(3):669–700, 2011.

[15] L. Chuan, Z. Jianxun, and N. Jing. Numerical and experimental analysis of residual stresses in full-penetration laser beam welding of ti6al4v alloy. *Rare metal materials and Engineering*, 38(8):1317–1320, 2009.

[16] S. Coulombe and J.L. Meunier. Arc-cold cathode interactions: parametric dependence on local pressure. *Plasma Sources Science and Technology*, 6(4):508, 1997.

[17] S. Coulombe and J.L. Meunier. Themo-field emission : a comparative study. *J. Phys. D: Appl. Phys*, 30:776–780, 1997.

[18] R.O. Dendy. *Plasma Dynamics*. Oxford Science Publications. Clarendon Press, 1990.

[19] R.H. Fowler and L.W. Nordheim. Electron emission in intense electric fields. *Proceedings of the Royal Society of London. Series A*, 119(781):173–181, 1928.

[20] P. Freton, J.J. Gonzalez, Z. Ranarijaona, and J. Mougenot. Energy equation formulations for two-temperature modelling of thermal plasmas. *Journal of Physics D: Applied Physics*, 45(46):465206, 2012.

[21] A.A. Fridman and L.A. Kennedy. *Plasma Physics and Engineering*. Taylor & Francis, 2004.

[22] A. Gleizes, B. Chervy, and J.J Gonzalez. Calculation of a two-temperature plasma composition: bases and application to sf6. *Journal of Physics D: Applied Physics*, 32(16):2060, 1999.

[23] D. Godin and J.Y Trépanier. A robust and efficient method for the computation of equilibrium composition in gaseous mixtures. *Plasma chemistry and plasma processing*, 24(3):447–473, 2004.

[24] R. J. Goldston and P.H. Rutherford. *Introduction to Plasma Physics*. Plasma Physics Series. Institute of Physics Pub., 1995.

[25] A.E. Guile. Arc-electrode phenomena. *Electrical Engineers, Proceedings of the Institution of*, 118(9):1131–1154, 1971.

[26] G.N. Haddad and A.J.D. Farmer. Temperature measurements in gas tungsten arcs. *Welding Journal*, 64(12):339–342, 1985.

[27] J. Haidar. A theoretical model for gas metal arc welding and gas tungsten arc welding. i. *Journal of applied physics*, 84(7):3518–3529, 1998.

[28] J. Haidar. Non-equilibrium modelling of transferred arcs. *Journal of Physics D: Applied Physics*, 32(3):263, 1999.

[29] D. Hastings and H. Garrett. *Spacecraft-Environment Interactions*. Cambridge Atmospheric and Space Science Series. Cambridge University Press, 2004.

[30] K.C. Hsu, K. Etemadi, and E. Pfender. Study of the free-burning high-intensity argon arc. *Journal of Applied Physics*, 54(3):1293–1301, 1983.

[31] K.C. Hsu and E. Pfender. Analysis of the cathode region of a free-burning high intensity argon arc. *Journal of Applied Physics*, 54(7):3818–3824, 1983.

[32] A. Javidi. Implementing chtmultiregionfoam solver for electric welding in openfoam 1.6.x, 2010. `http://www.tfd.chalmers.se/~hani/kurser/OS_CFD_2010/alirezaJavidi/alirezaReport.pdf`, 2013. [Online; accessed 19-May-2013].

[33] A. Javidi, I. Choquet, and H. Nilsson. Numerical modelling of shielding gas flow and heat transfer in laser welding process. In *Proceedings of The 5th International Swedish Production Symposium, Linköping, Sweden*, pages 269–276, 2012.

[34] A. Kramida, Yu. Ralchenko, Reader J., and NIST ASD Team. NIST Atomic Spectra Database (ver. 5.0). `http://physics.nist.gov/asd`, 2013. [Online; accessed 14-January-2013].

[35] H.J. Kunze. *Introduction to Plasma Spectroscopy (Springer Series on Atomic, Optical, and Plasma Physics)*. Springer, 2009.

[36] F. Lago, J.J Gonzalez, P. Freton, and A. Gleizes. A numerical modelling of an electric arc and its interaction with the anode: Part i. the two-dimensional model. *Journal of Physics D: Applied Physics*, 37(6):883, 2004.

[37] S. Lichtenberg, L. Dabringhausen, O. Langenscheidt, and J. Mentel. The plasma boundary layer of hid-cathodes: modelling and numerical results. *Journal of Physics D: Applied Physics*, 38(17):3112, 2005.

[38] J.J. Lowke, P. Kovitya, and H.P. Schmidt. Theory of free-burning arc columns including the influence of the cathode. *Journal of Physics D: Applied Physics*, 25(11):1600, 1992.

[39] M. Mitchner and H. Kruger. *Partially Ionized Gases (Wiley series in plasma physics)*. John Wiley & Sons Inc, 1973.

[40] D. Nandelstadt, M. Redwitz, L. Dabringhausen, J. Luhmann, S Lichtenberg, and J Mentel. Determination of hid electrode falls in a model lamp iii: Results and comparison with theory. *Journal of Physics D: Applied Physics*, 35(14):1639, 2002.

[41] A.V. Phelps and Z.L. Petrovic. Cold-cathode discharges and breakdown in argon: surface and gas phase production of secondary electrons. *Plasma Sources Science and Technology*, 8(3):R21, 1999.

[42] A.V. Potapov. Chemical equilibrium of multitemperature systems. *High Temp.*, 8:48–51, 1966.

[43] M.A. Ramírez, G. Trapaga, and J. McKelliget. A comparison between two different numerical formulations of welding arc simulation. *Modelling and Simulation in Materials Science and Engineering*, 11(4):675, 2003.

[44] V. Rat, P. André, J. Aubreton, M.F. Elchinger, P. Fauchais, and A. Lefort. Transport properties in a two-temperature plasma: Theory and application. *Physical Review E*, 64(2):026409, 2001.

[45] V. Rat, A.B. Murphy, J. Aubreton, M.F. Elchinger, and P. Fauchais. Treatment of non-equilibrium phenomena in thermal plasma flows. *Journal of Physics D: Applied Physics*, 41(18):183001, 2008.

[46] K.U. Riemann. The Bohm criterion and sheath formation. *Journal of Physics D: Applied Physics*, 24(4):493, 2000.

[47] J.R. Roth. *Industrial Plasma Engineering: Volume 1: Principles*. Industrial Plasma Engineering: Principles. Taylor & Francis, 2002.

[48] M. Sass-Tisovskaya. *Plasma arc welding simulation with OpenFOAM*. Chalmers University of Technology, 2009.

[49] H. Schmitz and K.U. Riemann. Consistent analysis of the boundary layer of a saha plasma. *Journal of Physics D: Applied Physics*, 34(8):1193, 2001.

[50] H. Schmitz and K.U. Riemann. Analysis of the cathodic region of atmospheric pressure discharges. *Journal of Physics D: Applied Physics*, 35(14):1727, 2002.

[51] N. Stenbacka, I. Choquet, and K. Hurtig. Review of arc efficiency values for gas tungsten arc welding. 2012.

[52] S. Tashiro, M. Tanaka, and A.B. Murphy. Numerical analysis of non-equilibrium plasma property in anode boundary layer of argon gas tungsten arc. *Surface and Coatings Technology*, 205:S115–S119, 2010.

[53] S. Vacquié, M. Aubès, and EDF Club. *L'arc électrique*. Eyrolles Paris, 2000.

[54] M.C.M. Van de Sanden, P. Schram, A.G. Peeters, JAM. Van der Mullen, and GMW. Kroesen. Thermodynamic generalization of the saha equation for a two-temperature plasma. *Physical Review A*, 40:5273–5276, 1989.

[55] K. Weman. *Welding Processes Handbook*. Woodhead Pub., 2003.

[56] J. Wendelstorf. *Ab initio modelling of thermal plasma gas discharges (electric arcs)*. 2000.

[57] W. Zhang, C-H. Kim, and T. DebRoy. Heat and fluid flow in complex joints during gas metal arc welding-part i numerical model of fillet welding. *Journal of applied physics*, 95(9):5210–5219, 2004.

[58] X. Zhou and J. Heberlein. Analysis of the arc-cathode interaction of free-burning arcs. *Plasma Sources Science and Technology*, 3(4):564, 1999.

[59] X. Zhou, J. Heberlein, and E. Pfender. Theoretical study of factors influencing arc erosion of cathode. *Components, Packaging, and Manufacturing Technology, Part A, IEEE Transactions on*, 17(1):107–112, 1994.